

Biogeochemical dynamics in adjacent mesoscale eddies of opposite polarity

Benedetto Barone¹, Matthew J Church², Mathilde Eleonore Dugenne³, Nicholas J. Hawco⁴, Oliver Jahn⁵, Angelicque E. White¹, Seth G John⁶, Michael J. Follows⁵, Edward F. DeLong⁷, and David M. Karl⁸

¹University of Hawaii at Manoa

²University of Montana

³School of Ocean and Earth Science and Technology

⁴University of Hawaii at Mānoa

⁵MIT

⁶University of Southern California

⁷University of Hawaii

⁸U of Hawaii

November 23, 2022

Abstract

We examined the biogeochemical impact of pairs of mesoscale cyclones and anticyclones in spatial proximity (<200 km apart) in the North Pacific Subtropical Gyre. While previous studies have demonstrated that upwelling associated with the intensification of cyclonic eddies supplies nutrients to the euphotic zone, we find that cyclonic eddies in their mature stage sustain plankton growth by increasing the diapycnal flux of nutrients to the lower portion of the euphotic zone. This increased supply results from enhanced vertical gradients in inorganic nutrients due to erosion of the nutricline that accompanied plankton growth during eddy intensification. From a biological standpoint, increased nutrient flux was linked with expansion of eukaryotic phytoplankton biomass and intensification of the deep chlorophyll maximum layer. This perturbation in the plankton community was associated with increased fluxes of biominerals (opal and calcium carbonate) and isotopically enriched nitrogen in particles exported in the cyclone. The time-integrated effects of thermocline uplifts and depressions were predictable deficits and surpluses of inorganic nutrients and dissolved oxygen in the lower euphotic zone. However, the stoichiometry of changes in oxygen and inorganic nutrients differed from that predicted for production and consumption of phytoplankton biomass, consistent with additional biological processes that decouple changes in oxygen and nutrient concentrations. The dynamics revealed by this study may be a common feature of oligotrophic ecosystems, where mesoscale biogeochemical perturbations are buffered by the deep chlorophyll maximum layer, which limits the ecological impact of eddies in the well-lit, near-surface ocean.

Ταβλε 1. Στοιχειομετρψ ανδ δ¹⁵N σιγνατυρε οφ παρτιςυλατε ματτερ εξπορτεδ δυρινη ΜΕΣΟ-Σ^οΠΕ ςρυισε.

Station	SLA (cm)	POC:Mass (g C:g)	PIC:Mass (g CaCO ₃ :g)	PSi:Mass (g Si:g)	PIC:PC (mol:mol)	POC:PN (mol:mol)	POC:PSi (mol:mol)	PN:PSi (mol:mol)	PN:PIC (mol:mol)
1	-12.0	0.22 ±0.02	0.38 ±0.02	0.025 ±0.001	0.17 ±0.02	7.3 ±0.9	21 ±2	2.8 ±0.2	0.66 ±0.06

Station	SLA (cm)	POC:Mass (g C:g)	PIC:Mass		PSi:Mass (g Si:g)	PIC:PC (mol:mol)	POC:PN (mol:mol)	POC:PSi (mol:mol)	PN:PSi (mol:mol)	PN:PIC (mol:mol)
			(g CaCO ₃ :g)	(g CaCO ₃ :g)						
2	-10.5	0.23 ±0.02	0.29 ±0.02	0.027 ±0.002	0.13 ±0.01	6.4 ±0.4	20 ±2	3.2 ±0.2	1.05 ±0.08	
3	0.0	0.20 ±0.01	0.36 ±0.02	0.018 ±0.003	0.18 ±0.01	6.6 ±0.8	25 ±5	3.8 ±0.8	0.70 ±0.08	
4	2.8	0.27 ±0.02	0.30 ±0.03	0.017 ±0.001	0.12 ±0.01	6.2 ±0.4	37 ±2	6.0 ±0.5	1.21 ±0.14	
5	8.0	0.24 ±0.02	0.35 ±0.01	0.021 ±0.003	0.15 ±0.01	6.6 ±0.6	26 ±4	4.0 ±0.7	0.87 ±0.06	
6	12.9	0.31 ±0.02	0.25 ±0.02	0.016 ±0.002	0.09 ±0.01	6.0 ±0.3	46 ±6	7.6 ±1.0	1.75 ±0.10	
7	17.4	0.29 ±0.02	0.25 ±0.01	0.016 ±0.002	0.10 ±0.00	5.8 ±0.6	43 ±5	7.4 ±1.0	1.64 ±0.15	
8	20.1	0.33 ±0.03	0.23 ±0.01	0.015 ±0.002	0.08 ±0.01	5.6 ±0.7	52 ±7	9.3 ±1.4	2.04 ±0.22	
9	22.8	0.34 ±0.03	0.26 ±0.02	0.010 ±0.001	0.08 ±0.01	5.8 ±0.5	78 ±8	13 ±1.2	1.90 ±0.12	
10	24.2	0.34 ±0.04	0.31 ±0.01	0.017 ±0.003	0.10 ±0.01	6.5 ±1.0	47 ±10	7.2 ±1.5	1.40 ±0.15	
11	24.7	0.33 ±0.04	0.28 ±0.04	0.015 ±0.001	0.09 ±0.02	6.0 ±1.1	53 ±7	8.8 ±1.3	1.61 ±0.31	
12	24.5	0.32 ±0.03	0.28 ±0.02	0.013 ±0.002	0.10 ±0.01	5.8 ±0.5	58 ±8	10.0 ±1.3	1.60 ±0.11	
Slope (units cm ⁻¹)		0.0038 ±0.0005	- 3.4·10 ⁻³ ±0.9·10 ⁻³	- 3.6·10 ⁻⁴ ±0.6·10 ⁻⁴	-0.0025 ±0.0005	-0.036 ±0.008	1.3 ±0.2	0.24 ±0.04	0.040 ±0.008	
r		0.90	-0.62	-0.86	-0.80	-0.73	0.85	0.84	0.80	
p		6.4·10 ⁻⁵	0.033	2.9·10 ⁻⁴	0.0019	0.0067	4.3·10 ⁻⁴	5.4·10 ⁻⁴	0.0019	

Hosted file

table_s1_gbcsubmission.docx available at <https://authorea.com/users/541464/articles/600627-biogeochemical-dynamics-in-adjacent-mesoscale-eddies-of-opposite-polarity>

Hosted file

si_barone_church_etal_gbcsubmission.docx available at <https://authorea.com/users/541464/articles/600627-biogeochemical-dynamics-in-adjacent-mesoscale-eddies-of-opposite-polarity>

1 Biogeochemical dynamics in adjacent mesoscale eddies of opposite polarity

2

3 Benedetto Barone^{1,2*}, Matthew J. Church^{3*}, Mathilde Dugenne^{1,2}, Nicholas J. Hawco^{4,2}, Oliver
4 Jahn⁵, Angelicque E. White^{1,2}, Seth G. John⁴, Michael J. Follows⁵, Edward F. DeLong^{1,2}, and
5 David M. Karl^{1,2}

* These authors contributed equally

¹ Daniel K. Inouye Center for Microbial Oceanography: Research and Education, University of
Hawai'i at Mānoa, Honolulu, Hawai'i, United States of America

² Department of Oceanography, University of Hawai'i at Mānoa, Honolulu, Hawai'i, United
States of America

³ Flathead Lake Biological Station, University of Montana, Polson, Montana, United States of
America

⁴ Department of Earth Sciences, University of Southern California, Los Angeles, California,
United States of America

⁵ Department of Earth, Atmospheric and Planetary Sciences, Massachusetts Institute of
Technology, Cambridge, Massachusetts, United States of America

Running title: Biogeochemical dynamics in adjacent eddies

Keywords: Mesoscale eddy; deep chlorophyll maximum; nutrient injection; diapycnal mixing;
chemical wake

Correspondence to: B. Barone; benedetto.barone@gmail.com; M. J. Church;
matt.church@flbs.umt.edu

6 **Key points**

7 - The steepness of the nutricline in mature mesoscale eddies is an important driver of the

8 variability of pelagic ecosystems

9 - Differences in eukaryotic phytoplankton communities alter the export of calcium carbonate and

10 opal containing particles across eddies

11 - Relative changes in oxygen and nutrients linked with displacements of the thermocline are

12 inconsistent with the cycling of organic matter

13

14 **Abstract**

15 We examined the biogeochemical impact of pairs of mesoscale cyclones and anticyclones in
16 spatial proximity (<200 km apart) in the North Pacific Subtropical Gyre. While previous studies
17 have demonstrated that upwelling associated with the intensification of cyclonic eddies supplies
18 nutrients to the euphotic zone, we find that cyclonic eddies in their mature stage sustain plankton
19 growth by increasing the diapycnal flux of nutrients to the lower portion of the euphotic zone.
20 This increased supply results from enhanced vertical gradients in inorganic nutrients due to
21 erosion of the nutricline that accompanied plankton growth during eddy intensification. From a
22 biological standpoint, increased nutrient flux was linked with expansion of eukaryotic
23 phytoplankton biomass and intensification of the deep chlorophyll maximum layer. This
24 perturbation in the plankton community was associated with increased fluxes of biominerals
25 (opal and calcium carbonate) and isotopically enriched nitrogen in particles exported in the
26 cyclone. The time-integrated effects of thermocline uplifts and depressions were predictable
27 deficits and surpluses of inorganic nutrients and dissolved oxygen in the lower euphotic zone.
28 However, the stoichiometry of changes in oxygen and inorganic nutrients differed from that
29 predicted for production and consumption of phytoplankton biomass, consistent with additional
30 biological processes that decouple changes in oxygen and nutrient concentrations. The dynamics
31 revealed by this study may be a common feature of oligotrophic ecosystems, where mesoscale
32 biogeochemical perturbations are buffered by the deep chlorophyll maximum layer, which limits
33 the ecological impact of eddies in the well-lit, near-surface ocean.

34 **1. Introduction**

35 Subtropical gyres are the dominant circulation features in all major ocean basins (Pedlosky,
36 1990), enclosing large biomes that cover ~40% of the Earth's surface (McClain et al., 2004).
37 Ecological variability in the subtropical gyres is closely linked to physical variability driven by
38 ocean currents (Mackas et al., 1985), which are most energetic at the mesoscale (10s to 100s of
39 km; Munk 2002) where the circulation forms closed vortices called nonlinear mesoscale eddies
40 (Chelton et al., 2007). A prior study, from a fixed location in the North Pacific Subtropical Gyre
41 (NPSG), revealed eddies were present 30% of the time (Barone et al., 2019). Hence,
42 understanding how mesoscale eddies impact pelagic ecosystem functioning in subtropical gyres
43 is an important step to identify the main drivers of biogeochemical variability in these expansive
44 biomes.

45 Eddies exert direct influence on plankton biogeochemistry (Falkowski et al., 1991) through
46 vertical oscillations of the thermocline (Wunsch, 1997), with concomitant changes in the vertical
47 distributions of nutrients relative to the upper ocean light field. Cyclonic eddy uplift of the
48 thermocline can enhance the supply of inorganic nutrients to the upper water column, while
49 downward displacement of the thermocline in anticyclonic eddies can move the deep reservoir of
50 inorganic nutrients further away from the sunlit upper ocean (Venrick, 1990; McGillicuddy and
51 Robinson, 1997). The intensification phase of cyclonic eddies is a transient event most often
52 associated with active upwelling, delivering inorganic nutrients to the euphotic zone and
53 supporting phytoplankton production (Sweeney et al., 2003; Rii et al., 2008).

54 Satellite remote sensing has previously been leveraged to describe the impact of mesoscale
55 eddies on near-surface ocean plankton dynamics by analyzing spatial anomalies in chlorophyll
56 concentrations relative to the eddy field (Chelton et al., 2011; Gaube et al., 2014, Guo et al.,
57 2019). These mesoscale chlorophyll anomalies are caused by different processes including

58 horizontal stirring, vertical motions, and trapping and transport of water parcels, with different
59 processes driving the variability in different oceanic regions (Gaube et al., 2014, Guo et al.,
60 2019). While satellite-based approaches provide valuable insights into physical-biological
61 interactions associated with eddies, they are restricted to the near-surface ocean and do not
62 provide information on dynamics occurring in the deeper regions of the euphotic zone. This is
63 particularly important in stratified ecosystems where the surface mixed layer is shallower than the
64 euphotic zone, and phytoplankton dynamics occurring within vertically distinct layers of the
65 upper ocean can be uncoupled.

66 In this study, we focused on mesoscale eddies in the permanently stratified central NPSG.
67 This ecosystem is characterized by persistently low inorganic nutrients throughout the upper
68 ~100 m, where there is sufficient light to drive net primary production (Karl, 1999). In this
69 environment, phytoplankton communities are vertically segregated (Venrick, 1982; Venrick,
70 1999; Malmstrom et al., 2010), with populations in the near-surface waters distinct from those in
71 the lower portion of the euphotic zone (100-175 m). Low-light adapted phytoplankton
72 assemblages inhabit the deep chlorophyll maximum (DCM), a persistent feature in stratified
73 ocean ecosystems (Li et al., 2011; Malmstrom et al., 2010). In the NPSG, the vertical position of
74 the DCM is defined by time-varying changes in the depth of light penetration (Letelier et al.
75 2004) and it broadly marks the transition between nutrient-limited phytoplankton growth above it
76 and light-limited phytoplankton growth below it (Cullen, 2015). Increased light energy to the
77 lower euphotic zone during the summer months allows vertical expansion of the upper ocean
78 habitat available to phytoplankton, resulting in a downward vertical displacement of the DCM
79 into denser, more nutrient-enriched waters (Letelier et al., 2004). In an analogous way, through
80 changes in the depth of isopycnal surfaces across an exponential attenuation in light flux,

81 mesoscale dynamics structure the vertical positioning of the DCM phytoplankton community,
82 with the DCM forming along colder, denser waters during periods of isopycnal uplift, such as
83 those driven by cyclonic eddies (Falkowski et al., 1991; McGullicuddy et al. 1999; Letelier et al.
84 2000; Vaillancourt et al. 2003; Kuwahara et al. 2008).

85 The main objective of this research was to better define the impacts that mesoscale eddies
86 have on the near-surface and DCM plankton communities. To do so, we sampled adjacent eddies
87 with opposite polarity, cyclonic and anticyclonic, in close spatial proximity during two research
88 cruises conducted in 2016 and 2017. Studying adjacent eddies permitted direct comparison of
89 these features without complications due to larger-scale horizontal variability. The eddies
90 sampled as part of these cruises represented extreme mesoscale events for this region (Barone et
91 al. 2019), providing new information on biogeochemical and plankton dynamics associated with
92 strong mesoscale perturbations. The generality of the biogeochemical and ecological responses
93 observed in these strong eddies was subsequently evaluated by leveraging the Eulerian
94 observations of the Hawaii Ocean Time-series (HOT) program and through comparisons with a
95 global ecosystem model.

96

97 **2. Material and methods**

98 *2.1 Identification of eddies*

99 We sampled adjacent eddies of opposite polarity during two oceanographic expeditions:
100 HOE-Legacy 4 (HL4) aboard the R/V *Ka`imikai-O-Kanaloa* (May 9-14, 2016); and MESO-
101 SCOPE aboard the R/V *Kilo Moana* (June 26-July 15, 2017). Eddies were identified as minima
102 (cyclones) and maxima (anticyclones) in sea level anomalies (SLA) based on a combination of all
103 available satellite altimetry products distributed by the Copernicus Marine Environment
104 Monitoring Service (<http://marine.copernicus.eu>). The SLA products were corrected for

105 interannual trends and seasonal cycles following procedures recently proposed for the nearby
106 Station ALOHA (Barone et al., 2019), located at 22° 45' N and 158° W; the resulting corrected
107 SLA is henceforth termed SLA_{corr} .

108 Prior to each cruise, maxima and minima in SLA_{corr} in waters north of the Hawaiian Islands
109 were monitored for several weeks; the selection of eddies to sample for these cruises included
110 consideration of proximity to Station ALOHA (for historical context and logistical
111 considerations), the strength of the adjacent eddies (based on SLA_{corr}), and assessment of time-
112 varying eddy behavior (e.g., strengthening or weakening in SLA_{corr}). Eddy coordinates, age, and
113 amplitude were tracked in time using a simple algorithm: For each daily map of SLA_{corr} , the eddy
114 center was defined as the minimum or maximum of SLA_{corr} in a square with a side of 1.5°
115 centered on the coordinates of the eddy center on the previous day. The amplitude of an eddy was
116 defined as the value of SLA_{corr} at the minimum or maximum. The age of each eddy was defined
117 as the number of days since the time of first detection, which was subjectively assessed as the
118 first day when a minimum or maximum detached from a larger area of positive or negative
119 SLA_{corr} . Similarly, the last day of eddy detection was subjectively defined as the day when a
120 minimum or maximum of SLA_{corr} could no longer be distinguished within a larger region with
121 positive or negative SLA_{corr} .

122 While we adopted a simplified tracking algorithm to describe eddy life history, eddies are
123 also routinely catalogued and tracked within the mesoscale eddy trajectory atlas (Schlax and
124 Chelton, 2016) distributed by AVISO+ (Archiving, Validation and Interpretation of Satellite
125 Ocean data; doi: 10.24400/527896/a01-2021.001). The four eddies sampled in this study were all
126 reported in the eddy atlas, but the MESO-SCOPE cyclone was considered as a single feature
127 together with a second cyclonic eddy during part of its lifetime. However, the trajectory of the

128 surface drifters (described in section 2.5) deployed during MESO-SCOPE showed cyclonic
129 circulation around the SLA_{corr} minimum defined as the eddy center in this study, hence it is likely
130 that the two minima which were merged in the eddy atlas represented distinct features.

131 *2.2 Water sampling and profiling instruments*

132 During transit, the hydrographic characteristics were measured using underway
133 conductivity, temperature, and depth (CTD) profilers (underway CTD, Teledyne), while current
134 speed and direction were measured using hull-mounted acoustic doppler current profilers (ADCP,
135 Workhorse 300 kHz, Teledyne). Upper ocean biogeochemical properties were characterized
136 using a rosette system mounting 10 L Niskin® sampling bottles and profiling instruments
137 including a CTD sensor (Sea-Bird 9/11 plus), a chlorophyll fluorometer (Seapoint SCF), a
138 polarographic oxygen (O_2) sensor (SBE 43, Sea-Bird), and a transmissometer (c-star, Sea-Bird).
139 In situ chlorophyll fluorescence was calibrated using a linear regression against the concentration
140 of chloropigments (comprised mostly of monovinyl and divinyl forms of chlorophyll *a* and *b*),
141 measured fluorometrically. Similarly, the O_2 sensor was calibrated from a linear regression of
142 dissolved O_2 concentrations determined at discrete depths measured using a Winkler titration
143 system (see below). Beam attenuation measurements that exceeded three standard deviations
144 from the mean based on 20 m vertical bins were removed in order to exclude observations
145 presumably due to rare, large particles. Furthermore, to account for variations in sensor
146 background values among deployments, the minimum value measured between 350-400 m was
147 subtracted from each beam attenuation profile (this approach assumes that particle scattering is
148 constant in the 350-400 m layer).

149 Light flux at discrete depths was calculated as the product of the daily-integrated
150 downwelling cosine PAR irradiance above the sea surface measured with a shipboard sensor (LI-

151 COR LI-190), and the fraction of downwelling PAR penetrating at depth measured using a free-
152 falling optical profiler (Sea-Bird Hyperpro II).

153 *2.3 Eddy transects*

154 Physical and biogeochemical characterizations of each of the eddy couples were obtained
155 by shipboard sampling along an approximately linear transect crossing both eddy centers (Figure
156 1a,b). An initial physical characterization was obtained while transiting using the ADCP and the
157 underway CTD. Biogeochemical observations were obtained at a lower horizontal resolution
158 along transects including 5 stations in 2016 and 11 stations in 2017, where measurements were
159 collected using the CTD rosette sampler. For these stations, hydrography and other profiling
160 sensor observations were measured using the instruments attached to the CTD rosette.

161 During HL4 (in 2016) there was a failure of the conductivity sensor that prevented an
162 accurate determination of salinity; hence, for this cruise only temperature observations from the
163 underway CTD are presented. Since this problem only impacted the underway instrument,
164 measurements of salinity and potential density associated with the biogeochemical observations
165 were still available from CTD measurements collected when the ship was stationary.

166 *2.4 High vertical resolution sampling*

167 In the four eddy centers, the layer surrounding the DCM was characterized using high
168 vertical resolution sampling (approximately 5 m vertical intervals) at 15 discrete depths around
169 the DCM (6 depths above the DCM, 8 depths below the DCM, in addition to the DCM). The
170 DCM was identified during each CTD deployment as the depth of the fluorescence maximum
171 (ranging from 96 to 151 m). This sampling was consistently done at 0700 local time to account
172 for possible diel variability in biogeochemical properties. The objective of this high vertical

173 resolution sampling was to characterize changes in water chemistry and plankton community
174 composition above, within, and below the DCM.

175 *2.5 MESO-SCOPE Lagrangian sampling*

176 During the 2017 expedition, we extended our observations through Lagrangian sampling of
177 the eddy centers using surface velocity program (SVP, Pacific Gyre) drifters with a drogue
178 centered at 15 m depth. Initially, eddy centers were identified using shipboard ADCP
179 measurements of upper ocean currents and underway hydrographic characterization conducted
180 while transiting across the eddies. Using this information, a SVP drifter was deployed in the
181 predicted center of each eddy (lowest current velocity and deepest or shallowest isopycnal depth).
182 These drifters advanced in arcs consistent with the geostrophic flow. A second SVP drifter was
183 then deployed near the center of the drift arcs to decrease the distance from the eddy center. The
184 research vessel followed these secondary drifters conducting high-temporal resolution
185 Lagrangian sampling over 3-4 days. The distance between the drifter and the ship at the
186 Lagrangian sampling stations averaged 1.1 ± 0.8 (standard deviation) km, with a maximum
187 distance of 4.1 km.

188 *2.6 Biogeochemical sample collection and analyses*

189 The analytical methods used for assessing upper ocean biogeochemical properties,
190 including concentrations of dissolved O₂, chlorophyll, dissolved and particulate nutrients, and
191 fluxes of particulate matter derived from sediment trap collections followed protocols utilized by
192 the HOT program (<http://hahana.soest.hawaii.edu/hot/methods/results.html>). Briefly,
193 concentrations of chlorophyll were determined from filtered seawater samples (25 mm diameter
194 glass fiber filters; Whatman GF/F, nominal porosity 0.7 μm). Concentrations of chlorophyll *a* and
195 phaeopigments were measured fluorometrically on a Turner Designs Model 10-AU fluorometer

196 (Strickland and Parsons, 1972). Note that, in this environment, fluorescence from chlorophyll *b* is
197 a major contributor to “phaeopigment” determinations (Karl et al., 2001). Seawater for
198 subsequent determinations of particulate carbon (PC) and nitrogen (PN) was prefiltered through
199 202 μm Nitex © mesh screen, followed by positive pressure filtration onto precombusted 25 mm
200 diameter glass fiber filters (Whatman GF/F). Filters were frozen at -20°C until analysis in the
201 laboratory. PC and PN concentrations were determined using an Exeter Analytical CE-440 CHN
202 elemental analyzer (Exeter Analytical, UK) as described in Grabowski et al. (2019).

203 Samples for the determination of dissolved O_2 were collected into borosilicate flasks, fixed
204 with manganous chloride and alkaline iodide, acidified, and dissolved O_2 concentrations were
205 determined by titration with thiosulfate (Carpenter, 1965). Water samples for subsequent
206 determinations of the sum of nitrate plus nitrite (hereafter N + N) and soluble reactive
207 phosphorus (herein termed phosphate, PO_4^{3-}) concentrations were collected in acid-washed
208 polyethylene bottles and stored frozen until analyzed (Dore et al., 1996) using a Bran Luebbe
209 Autoanalyzer III. For most samples where N+ N concentrations were below 100 nM,
210 concentrations were determined using a chemiluminescent method (Foreman et al. 2016).

211 Iron (Fe) was sampled using a trace metal clean rosette and analyzed by inductively
212 coupled plasma mass spectrometry after preconcentration by an automated SeaFAST system
213 (Elemental Scientific; see Hawco et al., companion submission, for full description).

214 *2.7 Calculation of isopycnal anomalies and nutrient gradients*

215 We calculated isopycnal concentration anomalies for inorganic nutrients and O_2 for both
216 HL4 and MESO-SCOPE cruises to illustrate biogeochemical changes driven by past physical-
217 biological processes in mesoscale eddies. These anomalies represent the concentrations of N+N,
218 PO_4^{3-} , and O_2 measured along an isopycnal surface minus the cruise-averaged concentrations

219 measured on the same isopycnal. Computing anomalies in this manner assumes similar initial
220 concentrations of nutrients and O₂ for a given isopycnal surface, and that mesoscale physical-
221 biological linkages drive variations in these properties.

222 Vertical gradients in inorganic nutrient concentrations were calculated as the slope of
223 Model I linear regressions of nutrient concentration versus depth at depths between 10 meters
224 above the DCM and down to 90 m below the DCM from individual nutrient profiles collected
225 during HL4 and MESO-SCOPE.

226 Isopycnal nutrient anomalies and vertical nutrient gradients were compared to near-monthly
227 Eulerian observations conducted by the HOT program at Station ALOHA. These HOT program
228 observations (1988-2020) were used to examine the relationships between SLA_{corr} and the O₂ and
229 inorganic nutrient anomalies along the 24.5 kg m⁻³ isopycnal surface (henceforth we refer to an
230 isopycnal surface based on its potential density anomaly, which is the potential density - 1000 kg
231 m⁻³). For these analyses, we eliminated potential seasonal variability in O₂ and inorganic nutrient
232 concentrations by subtracting the monthly mean isopycnal concentrations of these properties.
233 When comparing these anomalies with those observed during the HL4 and MESO-SCOPE
234 cruises, for consistency we subtracted the HOT monthly mean concentration also from the
235 isopycnal anomalies calculated on the eddy transects.

236 The calculation of vertical nutrient gradients on HOT observations followed the same
237 procedure described for HL4 and MESO-SCOPE. Vertical profiles where less than 3
238 measurements existed in the vertical layer around the DCM were discarded for these analyses.

239 *2.8 Plankton abundance and biomass*

240 Abundances of picocyanobacteria (*Prochlorococcus* and *Synechococcus*) and pigmented
241 eukaryotes (pico- and nanoplankton), together with non-pigmented picoplankton (hereafter

242 heterotrophic bacteria), were determined by flow cytometry. For these analyses, seawater was
243 collected in 2 mL cryovials, fixed with microscopy-grade paraformaldehyde (0.24% vol/vol final
244 concentration), stored in the dark for 15 min, flash frozen in liquid nitrogen, and stored at -80 °C.
245 Plankton were enumerated with an Influx (Cytocpeia) flow cytometer, with pigmented cells
246 distinguished based on their scattering and fluorescence characteristics using two excitation lasers
247 (457 and 488 nm). The abundance of non-pigmented picoplankton (herein defined as
248 heterotrophic bacteria) was determined by staining cells with SYBR Green I DNA and
249 subtracting the contributions from *Prochlorococcus*.

250 The carbon biomass of larger (4-100 µm) eukaryotic phytoplankton was estimated by
251 automated imaging flow cytometry (Imaging FlowCytobot [IFCb], McLane) over the course of
252 the Lagrangian sampling in 2017. In both eddy centers, daily discrete samples were collected
253 every 4 hours (n=6 at each depth) at 15 m and at the DCM from Niskin® bottles mounted on the
254 CTD rosette. Analyses were carried out within 2 hours of collection to ensure that cells were not
255 deteriorating since samples were not preserved. The IFCb detects individual particles via laser-
256 induced fluorescence and light scattering used to trigger image acquisition of all particles in
257 successive ~5 mL samples.

258 A training set was used to classify the images to the genus level based on morphological
259 traits, as described in Dugenne et al. (2020). The output of the random forest classifier (Sosik and
260 Olson, 2007) was manually corrected to provide accurate estimates of cell size distribution and
261 concentration for individual genera. For this study, we selected phytoplankton genera, then
262 computed carbon biomass based on a biovolume-to-C quota using class-specific regression
263 coefficients (Menden-Deuer and Lessard, 2000). Standard errors associated with the intercept and

264 slope of the biovolume-to-C regressions result in a $\pm 20\%$ uncertainty in larger phytoplankton
265 biomass.

266 *2.9 Quantification of particle export*

267 During the MESO-SCOPE cruise, 12 free-drifting sediment trap arrays were deployed
268 along a line connecting the eddy centers (at approximately 18 km spacing) to examine the
269 downward flux of sinking particulate material. Each surface-tethered array included 12 individual
270 particle interceptor trap collector tubes (Knauer et al. 1979). Traps were deployed at 150 m for 10
271 to 13 days, passively collecting sinking particles. The sediment traps were prepared and
272 processed following HOT program methods (Karl et al. 1996). Trap samples were processed and
273 analyzed for total mass, PC, PN, particulate phosphorus (PPO_4^{3-}), particulate silica (PSi),
274 particulate inorganic carbon (PIC; i.e., calcium carbonate), and stable nitrogen isotope
275 composition in particles ($\delta^{15}\text{N}$ -PN). From the 12 individual collector tubes, 6 were processed for
276 subsequent measurements of PC, PN, $\delta^{15}\text{N}$ -PN; 3 were processed for PPO_4^{3-} ; and the remaining 3
277 traps were split and processed for PIC, PSi, and total mass flux. Prior to filtration, trap contents
278 were screened through a 335- μm Nitex mesh to remove any mesozooplankton (swimmers) that
279 are not part of the passive flux of particles. Collection tubes for subsequent analyses of PC and
280 PN were filtered onto 25 mm diameter combusted glass fiber filters, while samples for PPO_4^{3-}
281 analyses were filtered onto combusted, acid-washed glass fiber filters. Samples for PSi and total
282 mass were filtered onto 47 mm diameter, 0.8 μm pore size polycarbonate filters, while PIC
283 samples were filtered onto 25 mm diameter, 0.2 μm pore size polycarbonate filters. All filters
284 were frozen until subsequent analyses. Filters for PC, PN, and $\delta^{15}\text{N}$ -PN were analyzed on a high-
285 temperature elemental analyzer (Carla Erba NC 2500) coupled to a Finnigan MAT DeltaS mass
286 spectrometer. Filters for total mass were analyzed as described in Karl et al. (1996). Filters for

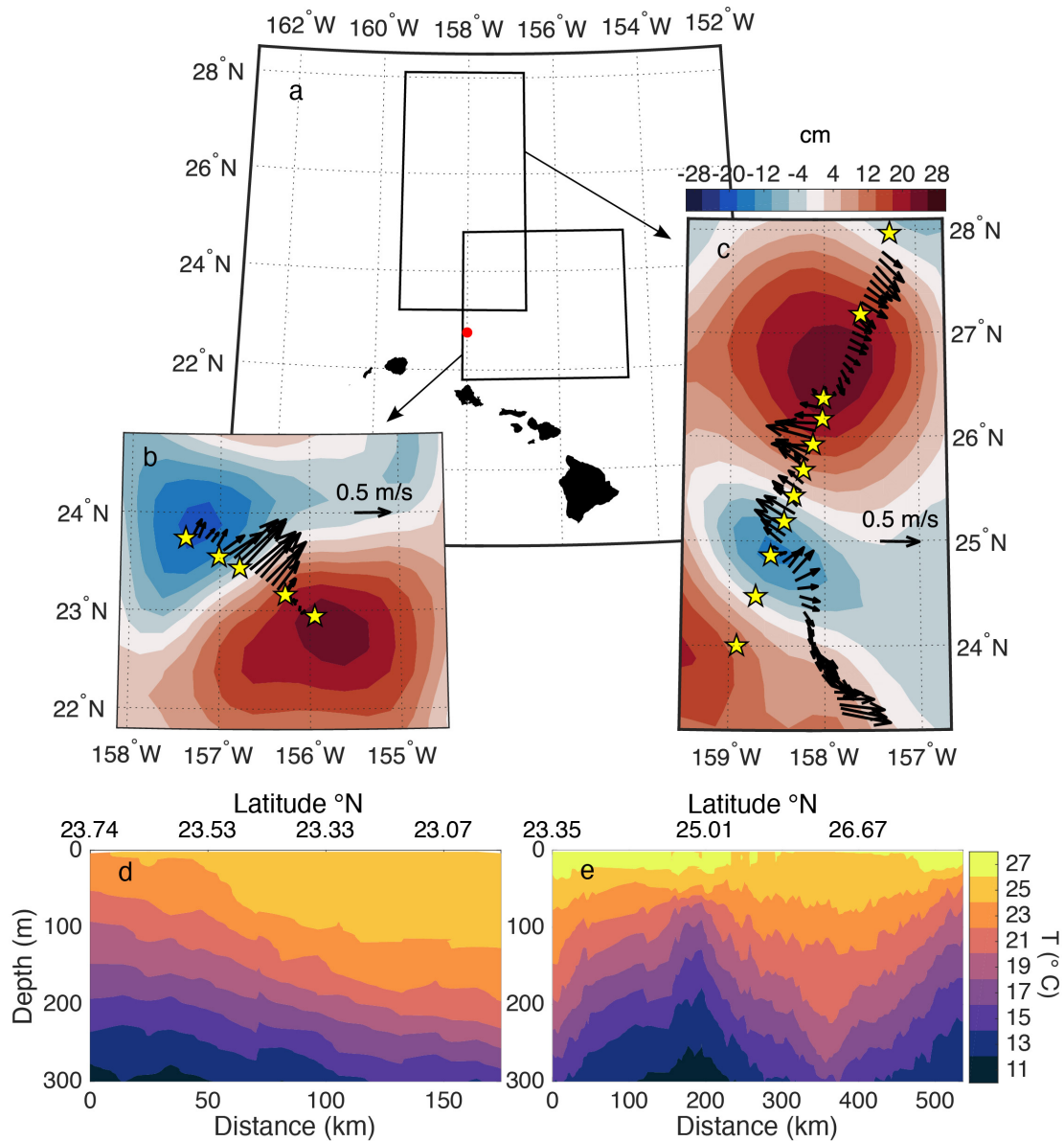
287 PIC determinations were placed in gas-tight vials, fumed with phosphoric acid, and the CO₂
288 evolved in the headspace quantified by infrared absorption (Grabowski et al., 2019). P_{Si} analyses
289 followed the NaOH digestion method for biogenic silica described in Brzezinski and Nelson
290 (1989). Particulate organic carbon (POC) flux was calculated as the difference between PC and
291 PIC.

292 *2.10 Numerical simulation of physical-biological dynamics at Station ALOHA*

293 We examined the relationships between nutrients, phytoplankton biomass, and SLA_{corr} in a
294 global simulation using the Massachusetts Institute of Technology General Circulation Model
295 (MITgcm; Marshall et al., 1997) and associated biogeochemical and ecological components as
296 detailed by Dutkiewicz et al. (2015) but with increased resolution in phytoplankton diversity. The
297 eddy-permitting physical simulation has an effective resolution of 1/6° and horizontal grid of
298 ~18 km (ECCO2; <http://ecco2.jpl.nasas.gov/>; Menemenlis et al., 2008) which, at subtropical
299 latitudes, resolves mesoscale but not sub-mesoscale features. Briefly, the biogeochemical model
300 resolves cycles of carbon, phosphorus, nitrogen, silica, iron, and oxygen with inorganic, living,
301 dissolved and particulate organic phases. The configuration examined here resolves 35
302 phytoplankton types spanning several size classes within each of five broad functional classes
303 (diatoms, coccolithophorids, mixotrophs, nitrogen fixers, and pico-phytoplankton). Sixteen size-
304 differentiated types of zooplankton are resolved, but the population of heterotrophic decomposers
305 is implicit (Dutkiewicz et al, 2015). Physical and biogeochemical model codes are available at
306 <http://mitgcm.org> and <https://github.com/darwinproject/darwin3> respectively. Selected simulation
307 results are available at <http://simonscmap.org> (search term “Darwin”).

308 For this study, we extracted the simulation results at Station ALOHA with a temporal
309 resolution of 3 days and for a period of 23 years. We computed SLA_{corr} and dN/dz using the same

310 methods adopted for field observations. The biomass of eukaryotic phytoplankton was obtained
 311 by summing the biomass of all eukaryotic phytoplankton types, and the concentration of N+N
 312 was obtained as the sum of NO_3^- and NO_2^- , which are represented separately in the model.
 313



314
 315 **Figure 1:** Sampling across adjacent mesoscale eddies during the two expeditions described in this study. The ocean
 316 near the Hawaiian archipelago is depicted in a) with black boxes representing the regions sampled during HL4 and
 317 MESO-SCOPE, and the red circle representing the position of Station ALOHA. Contours of sea level anomaly are
 318 depicted in b) during HL4 (11 May 2016), and c) MESO-SCOPE (28 June 2017). Arrows depict the average current

319 velocity and direction measured from the research vessel with an acoustic doppler current profiler in the 11-61 m
320 depth layer; yellow stars depict the sampling stations along a transect where water samples were collected from the
321 ship. Temperature contours along the transects are shown in d) for HL4, and e) for MESO-SCOPE. Data from 2016
322 include both shipboard measurements and measurements collected with an underway profiling CTD system. Data
323 from 2017 include only measurements collected with an underway CTD.

324

325 **3. Results**

326 *3.1 Transects across adjacent eddies*

327 The hydrographic and dynamic structure of the sampled eddies was consistent with
328 expectations based on eddy polarity: cyclonic eddies were characterized by an uplifted
329 thermocline and surface currents organized in a counterclockwise circulation, while anticyclones
330 demonstrated deeper thermoclines and clockwise surface current circulation (Figure 1). In both
331 cruises, surface currents were strongest along the frontal boundaries separating the adjacent
332 eddies. During the HL4 cruise, frontal currents reached a maximum velocity of 0.85 m s^{-1} in the
333 11-61 m layer; during the MESO-SCOPE cruise in 2017 frontal currents reached a maximum
334 velocity of 0.60 m s^{-1} . High horizontal resolution underway CTD profiles conducted during HL4
335 revealed the depth of the 19°C isotherm varied from 120 m in the cyclone center to 244 m in the
336 anticyclone center (Figure 1d), while this isotherm varied between 79 m in the cyclone center to
337 255 m in the anticyclone center during MESO-SCOPE (Figure 1e). Similarly, the vertical
338 position of isopycnal surfaces varied with eddy polarity. For example, during the HL4 cruise in
339 2016, the depth of the 25 kg m^{-3} isopycnal surface (typically occurring near the base of the DCM
340 at Station ALOHA) deepened from 112 m near the cyclone center to 243 m near the anticyclone
341 center (Figure 2), while this isopycnal varied from 84 m near the cyclone center to 220 m near the
342 anticyclone center during the MESO-SCOPE cruise (Figure 2). This isopycnal was shallowest
343 (80 m) in the northernmost station of the MESO-SCOPE cruise transect, reflecting the low SLA

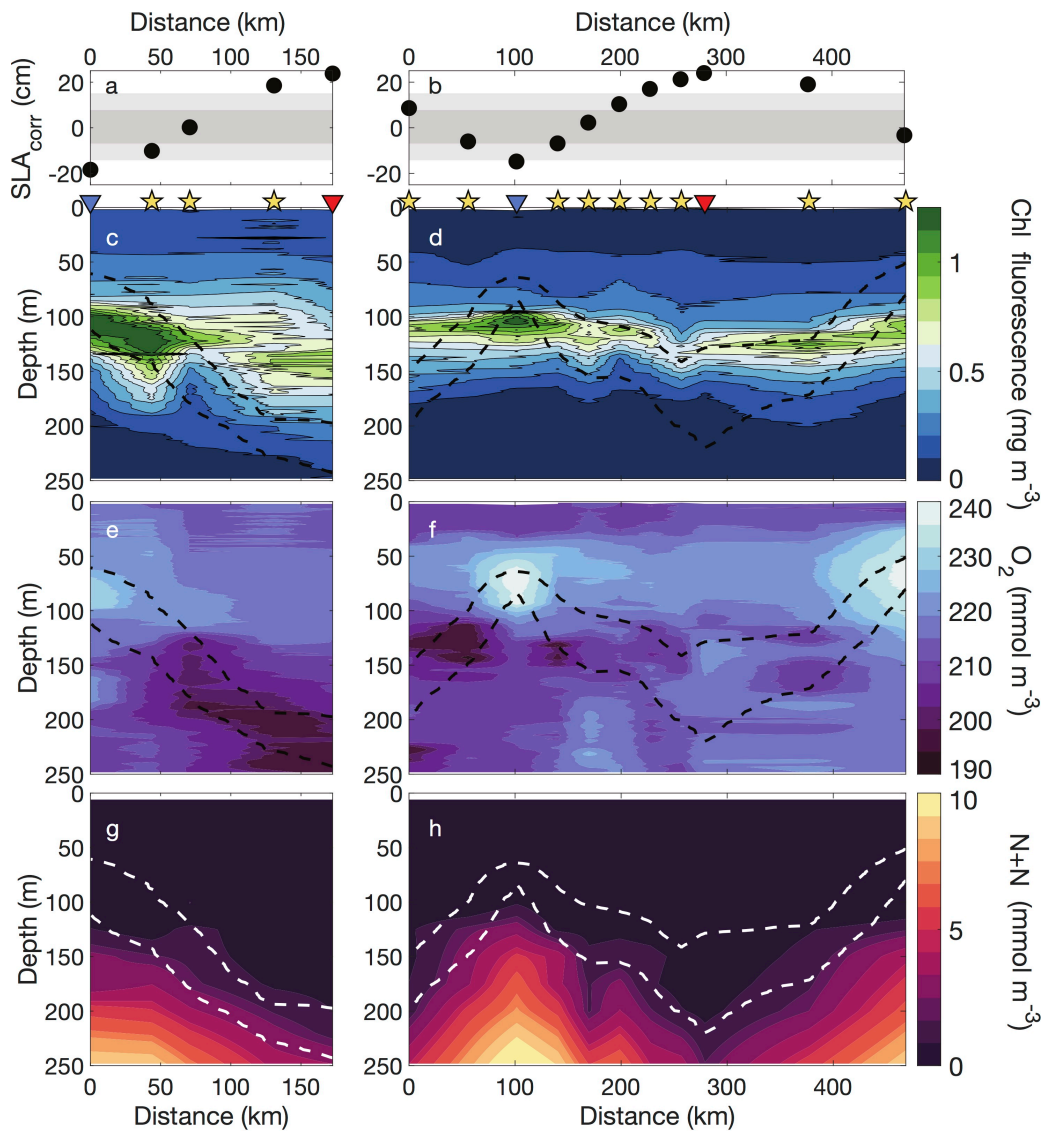
344 observed at this station, together with shallowing of isopycnals towards the northern edge of the
345 NPSG.

346 Both of the cyclones and anticyclones sampled as part of this study represented extreme
347 mesoscale events relative to historical Eulerian observations of SLA_{corr} at Station ALOHA
348 (Figure 2). SLA_{corr} in the cyclone and anticyclone eddy centers averaged -18.4 cm and 23.8 cm
349 during HL4 and -14.7 cm and 24.0 cm during MESO-SCOPE, respectively. In both cases, these
350 SLA_{corr} values were more than two standard deviations different from the mean SLA_{corr} measured
351 at Station ALOHA between 1993 and 2018 (Figure 2a,b).

352 The vertical position of the DCM also varied consistently with eddy polarity, with cyclones
353 characterized by shallower DCM, but more intense chlorophyll fluorescence relative to
354 anticyclones (Figure 2c,d). Moreover, during both cruises, but particularly during MESO-
355 SCOPE, concentrations of dissolved O_2 in the cyclones peaked at depths shallower than the
356 DCM, with O_2 concentrations greatest near the top of the 24.5 kg m^{-3} isopycnal in the cyclones,
357 despite the DCM occurring closer to the 25 kg m^{-3} isopycnal (Figure 2e,f). Concentrations of O_2
358 along the 24.5 kg m^{-3} isopycnal were greatest in the cyclone sampled during the MESO-SCOPE
359 cruise, peaking at $242.0 \text{ mmol m}^{-3}$ and decreasing to $220.9 \text{ mmol m}^{-3}$ in the center of the
360 anticyclone (Figure 2). O_2 concentrations measured across the eddies as part of HL4
361 demonstrated similar patterns, with a peak concentration of $232.7 \text{ mmol m}^{-3}$ just below the 24.5
362 kg m^{-3} isopycnal in the cyclone and decreasing to a maximum $218.8 \text{ mmol m}^{-3}$ in the center of
363 the anticyclone (Figure 2).

364 The observed eddy-dependent vertical changes in isopycnal surfaces resulted in
365 displacement of inorganic nutrient concentrations, with upward displacement of N+N
366 concentrations below the DCM in cyclones, and downward displacement of isopycnals in

367 anticyclones reducing concentrations of N+N throughout the upper 200 m (Figure 2g,h). N+N
 368 concentrations along the 24.5 kg m⁻³ were elevated in the anticyclones, ranging 0.976 and 0.026
 369 mmol m⁻³ during HL4 and MESO-SCOPE, respectively, with lower concentrations in both
 370 cyclones (< 0.003 mmol m⁻³; Figure 2). Along the 25 kg m⁻³ isopycnal, concentrations of N+N
 371 ranged between 0.002 and 2.975 mmol N m⁻³ during MESO-SCOPE, and between 3.584 and
 372 0.875 mmol N m⁻³ during HL4, across all stations.



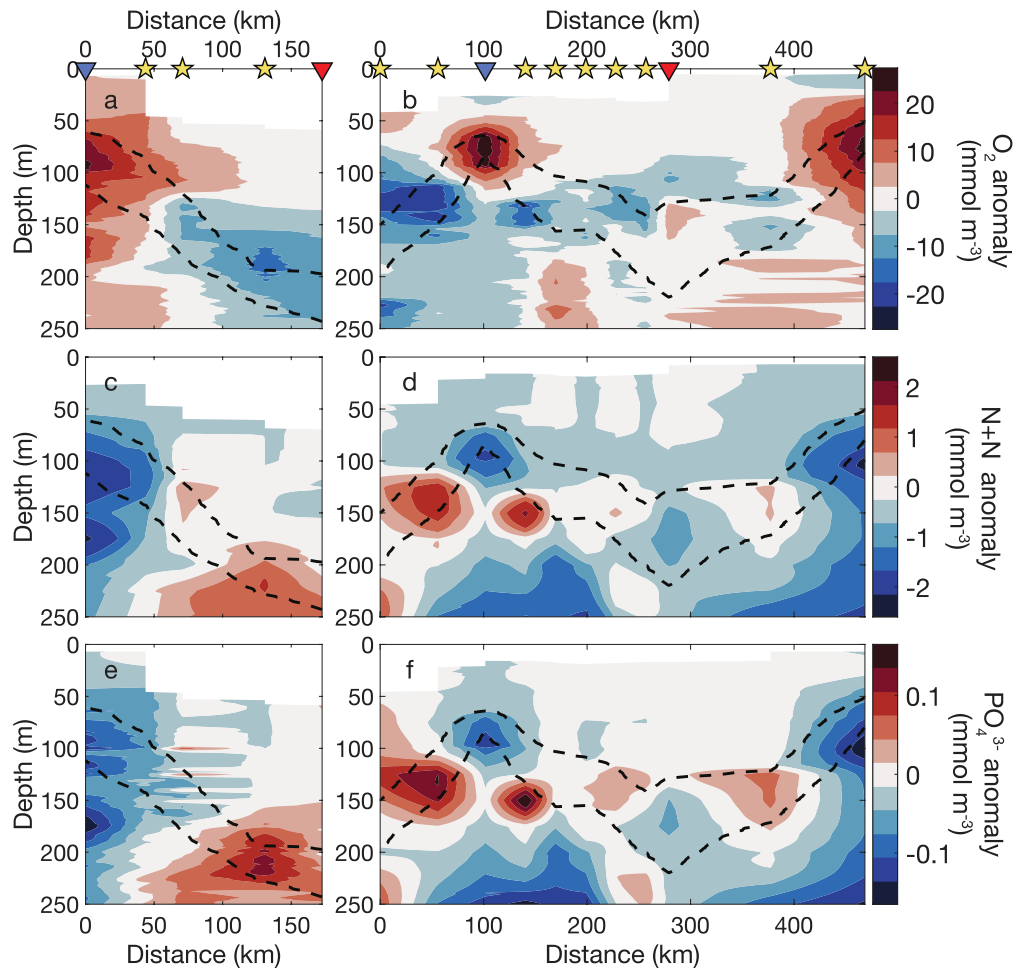
373
 374 **Figure 2:** Biogeochemical characteristics along two transects between the couple of adjacent eddies sampled during
 375 HL4 in 2016 (panels a,c,e,g) and MESO-SCOPE in 2017 (panels b,d,f,h). a,b) SLA_{corr} at stations sampled during
 376 transects across adjacent eddies (black symbols). Shaded areas represent variability in SLA_{corr} at Station ALOHA

377 between 1993 and 2018, with dark grey shading depicting ± 1 standard deviation of the mean and light grey shading
378 depicting ± 2 standard deviations from the time-averaged SLA_{corr} value; c,d) Chlorophyll (Chl) fluorescence (e,f),
379 dissolved O_2 concentrations (g,h), and concentrations of N+N during adjacent eddy sampling transects. Dashed lines
380 depict the depth of isopycnal surfaces with potential density anomaly of 24.5 kg m^{-3} (shallower surface), and 25 kg
381 m^{-3} (deeper surface). Symbols on the top panels depict the position of the sampling stations along the transects, with
382 blue and red triangles depicting the stations closest to the cyclone and the anticyclone centers, respectively.

383
384
385

3.2 Isopycnal anomalies of O_2 and inorganic nutrients

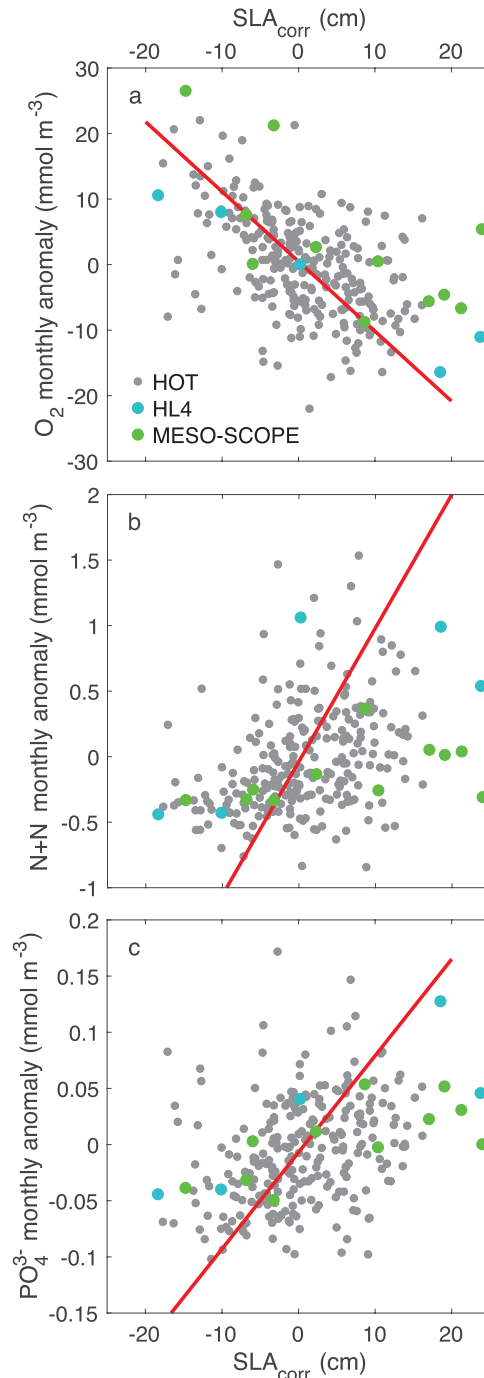
386 Depth-dependent oscillations in the thermocline appear to underlie much of the variability
387 associated with concentrations of inorganic nutrients and dissolved O_2 (Fig. 2g,h). However,
388 analyses of these properties along isopycnal surfaces revealed more subtle dynamics. For both
389 cruises, robust anomalies for both O_2 and inorganic nutrients were observed along isopycnal
390 surfaces located at depths surrounding the DCM. The isopycnal anomalies in cyclonic eddies
391 were consistently positive for O_2 (Figure 3a,b) and consistently negative for N+N and PO_4^{3-}
392 (Figure 3c-f), indicative of prior net phytoplankton production. Anomalies associated with
393 anticyclones demonstrated less robust mesoscale variation: for example, during the HL4
394 anticyclone anomalies associated with N+N, PO_4^{3-} , and O_2 near the DCM had the opposite sign
395 than those measured in the cyclone, while during MESO-SCOPE inorganic nutrient anomalies
396 near the DCM had the same sign in both the cyclone and anticyclone (Figure 3).



397
 398 **Figure 3:** Concentration anomalies of O₂ (a,b), N+N (c,d), and PO₄³⁻ (e,f) with respect to the mean isopycnal
 399 concentration measured during sampling transects of adjacent eddies during HL4 (a,c,e) and MESO-SCOPE (b,d,f).
 400 Dashed lines depict the depth of potential density anomaly isopycnal surfaces of 24.5 kg m⁻³ (shallower surface), and
 401 25 kg m⁻³ (deeper surface). Symbols on the top panels depict the position of the sampling stations along the transect,
 402 with blue and red triangles depicting the stations closest to the cyclone and the anticyclone centers, respectively.

403 To assess the generality of mesoscale variability in biogeochemistry along isopycnal
 404 surfaces located near the depth of the DCM, we evaluated relationships between SLA_{corr} and both
 405 O₂ and inorganic nutrient anomalies along the 24.5 kg m⁻³ surface using historical HOT program
 406 measurements (Figure 4). These analyses revealed consistent patterns in both the HOT program
 407 observations and the eddy transects. In particular, the seasonally detrended O₂ concentration
 408 anomalies decreased with increasing SLA_{corr}, while the de-seasoned concentration anomalies of

409 both N+N and PO₄³⁻ increased with SLA_{corr} (Figure 4). The consistency in concentrations of O₂
410 and inorganic nutrients to variations in SLA_{corr} along this isopycnal surface suggests the patterns
411 we observed are not specific to strong mesoscale eddies, but rather are more generally reflective
412 of the full range of mesoscale motions observed in the region near Station ALOHA. Slopes of the
413 isopycnal concentration anomalies versus SLA_{corr} (Model II geometric mean regression) were -
414 1.07 ± 0.07 mmol O₂ m⁻³ cm⁻¹, 0.102 ± 0.008 mmol N+N m⁻³ cm⁻¹ and 0.00860 ± 0.00067 mmol
415 PO₄³⁻ m⁻³ cm⁻¹. The resulting ratios of these slopes were -10.49 (mol O₂ : mol N), -124.4 (mol O₂
416 : mol P), and 11.86 (mol N : mol P). SLA_{corr} explained less of the variability in the inorganic
417 nutrient concentration anomalies than O₂ concentration anomalies (correlation coefficients values
418 for O₂, N+N, and PO₄³⁻ were -0.49, 0.21, and 0.23, respectively, with all $p < 0.001$), and this is
419 particularly noteworthy for N+N at low values of SLA_{corr} (i.e., when SLA_{corr} decreases below -10
420 cm, such as would occur with relatively strong cyclonic eddies). Potential Fe limitation of DCM
421 plankton production was also investigated during the MESO-SCOPE cruise and results from that
422 study are described elsewhere (Hawco et al., companion submission). Briefly, dissolved Fe was
423 depleted in the lower euphotic zone of the cyclone, averaging 73 nmol m⁻³ at a potential density
424 of ~25.16 kg m⁻³, the same isopycnal where we measured the maximum cyclonic deficit of N+N
425 and PO₄³⁻. In this layer, the cyclone had 110 nmol m⁻³ less Fe than the anticyclone as compared
426 with a 1.80 mmol m⁻³ and 0.11 mmol m⁻³ decreases in N+N and PO₄³⁻, respectively. Lower
427 dissolved Fe at 25.16 kg m⁻³ in the cyclonic eddy is consistent with biological Fe uptake by
428 phytoplankton.

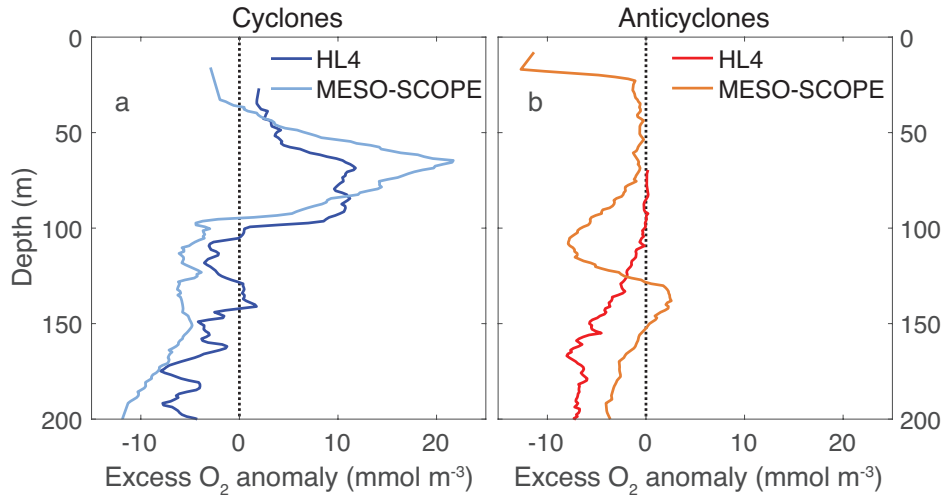


429
 430 **Figure 4:** Monthly isopycnal anomalies of the concentrations of O₂ (a), N+N (b), and PO₄³⁻ (c) versus SLA_{corr} from
 431 HOT program measurements (gray symbols), the HL4 eddy transect (blue symbols), and the MESO-SCOPE eddy
 432 transect (green symbols) along the 24.5 kg m⁻³ density surface. Red lines depict the Model II geometric mean
 433 regression of HOT observations. Note that for visual clarity the y-axes exclude three observations with high
 434 concentration anomalies of N+N (2.4, 4.4, and 8.2 mmol m⁻³ corresponding to SLA_{corr} of 8.4, -4.7, and 1.4 cm,
 435 respectively) and two observations with high concentration anomalies of PO₄³⁻ (0.28 and 0.56 mmol m⁻³
 436 corresponding to SLA_{corr} of -4.7, and 1.4 cm, respectively).

437 The isopycnal anomalies of O₂ and inorganic nutrients vary inversely due to primary
438 production and mineralization, which produce O₂ and consume inorganic nutrients (or vice versa)
439 in proportions that are relatively invariant across ocean basin scales (Redfield, 1958; Anderson
440 and Sarmiento, 1994). To assess if the isopycnal variations of O₂ and inorganic nutrients in
441 mesoscale eddies were consistent with the stoichiometry of the production and consumption of
442 organic matter, we calculated the excess O₂ anomaly as follows:

443 isopycnal anomaly of (O₂ - O_{2 solubility}) + 10.5 × isopycnal anomaly of (NO₃⁻ + NO₂⁻)

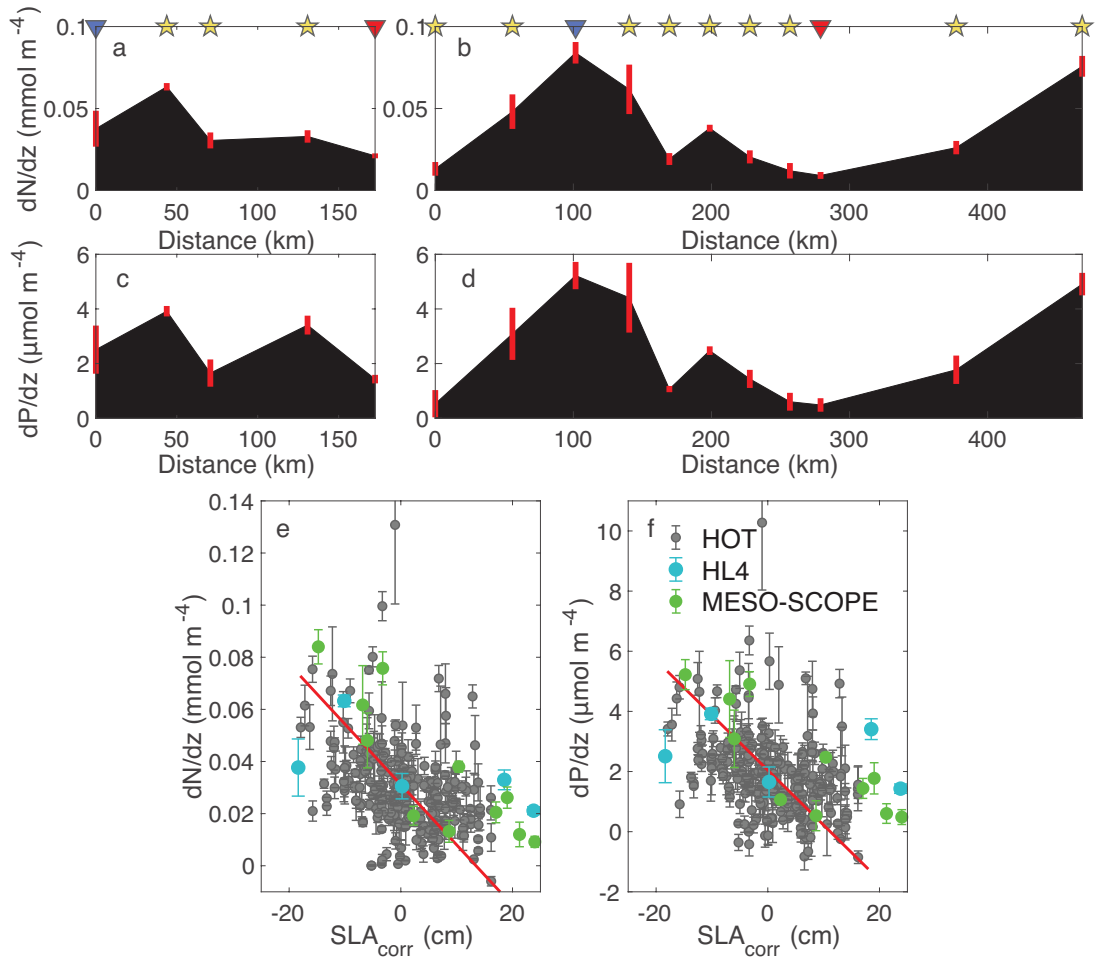
444 where 10.5 represents the moles of O₂ produced when 1 mole of NO₃⁻ + NO₂⁻ is consumed for the
445 synthesis of new organic matter, or the inverse for its consumption (Anderson, 1995; Johnson et
446 al., 2010). For this analysis, we also subtracted O₂ solubility to avoid misinterpreting variations
447 caused by changes in hydrography along the eddy transects. The excess O₂ anomaly was positive
448 in both cyclone centers in a vertical layer located just above the DCM and approximately
449 between 50 and 100 m (Figure 5a). In this layer, the excess O₂ anomaly reached values above 10
450 mmol m⁻³ in cyclones, while it was close to 0 or negative in both anticyclones (Figure 5). The
451 excess O₂ anomaly was predominantly negative below 100 m in all four eddy centers (Figure 5),
452 indicating that the O₂ concentration in these eddy centers was lower than expected assuming the
453 water started with the average isopycnal concentrations measured along the transect and was later
454 modified assuming fixed 10.5 O₂:N stoichiometry (Anderson, 1995).



455
 456 **Figure 5:** Excess O₂ anomaly in cyclones (a) and anticyclones (b). Excess O₂ anomaly reflects the surplus of O₂ with
 457 respect to the concentration expected if starting from the average isopycnal concentrations of O₂ and NO₃⁻ + NO₂⁻
 458 along the transects and assuming that they are modified following a fixed -10.5 O₂:N stoichiometry.

459 *3.3 Vertical gradients and mixing estimates at the top of the nutricline*

460 We calculated how mesoscale motions influenced vertical gradients in N+N and PO₄³⁻
 461 based on the slopes of nutrient concentration versus depth relationships calculated from the
 462 individual nutrient profiles. Upward displacement of the nutricline associated with cyclonic
 463 eddies resulted in vertical gradients in N+N that were 1.8 to 9.2 times greater near the center of
 464 the cyclones than in the anticyclones (Figure 6a,b). Similarly, vertical gradients in PO₄³⁻ were 1.8
 465 to 10.8 times greater near the center of the cyclones than in the anticyclones (Figure 6c,d). During
 466 both HL4 and MESO-SCOPE cruises, the maximum and minimum vertical gradients were
 467 observed at stations close to the centers of the cyclone and of the anticyclone, respectively
 468 (Figure 6a,c).



469
 470 **Figure 6:** Changes in the vertical gradients of N+N (a,b) and PO_4^{3-} (c,d), defined as dN/dz and dP/dz , respectively,
 471 across adjacent eddies of opposite polarity for HL4 (a,c) and MESO-SCOPE (b,d) cruises. Panels e-f depict vertical
 472 gradients in N+N and PO_4^{3-} concentrations, respectively, versus SLA_{corr} for the two eddy transects (blue and green
 473 symbols) and the HOT program observations (gray symbols). Red lines in a-d and error bars in e-f depict ± 1 standard
 474 deviation in the slopes. Red lines in e-f are linear regressions on HOT program nutrient gradients (Model II) with
 475 slopes of $-0.0023 \pm 0.0002 \text{ mmol m}^{-4} \text{ cm}^{-1}$ ($r=0.36$, $p=5 \cdot 10^{-9}$) and $-0.00018 \pm 0.00001 \text{ mmol m}^{-4} \text{ cm}^{-1}$ ($r=0.35$,
 476 $p=1 \cdot 10^{-8}$) for N+N and PO_4^{3-} , respectively. Estimates of vertical nutrient gradients were obtained by calculating the
 477 slope of the Model I linear regression of nutrient concentration versus depth in the vertical layer between 10 m above
 478 and 90 below the depth of the DCM.

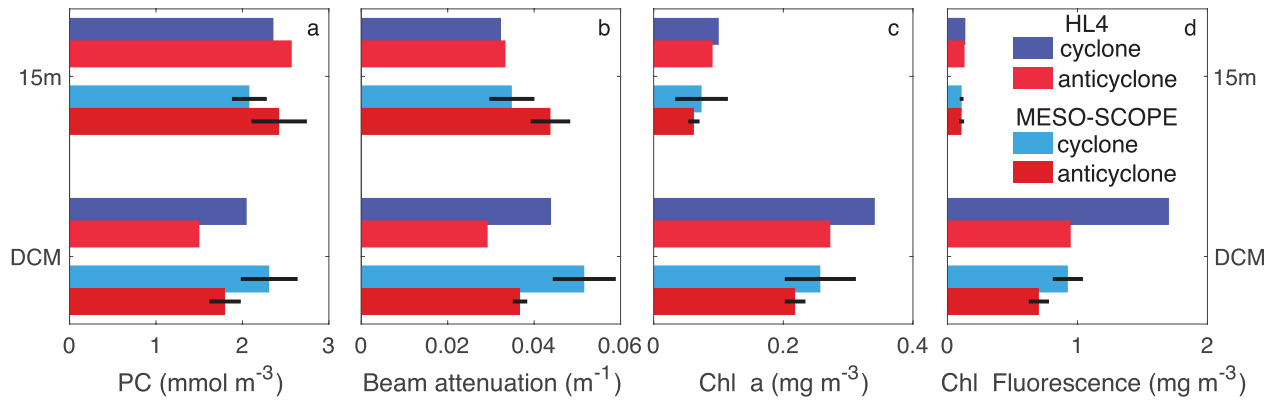
479 We also examined relationships between the vertical nutrient gradients and SLA_{corr} based
 480 on the historical HOT program observations (Fig 6e,f). These analyses revealed patterns
 481 consistent with the more limited observations during HL4 and MESO-SCOPE. Specifically,

482 vertical gradients in concentrations of $N+N$ and PO_4^{3-} decreased with increases in SLA_{corr} (Fig
483 6e,f).

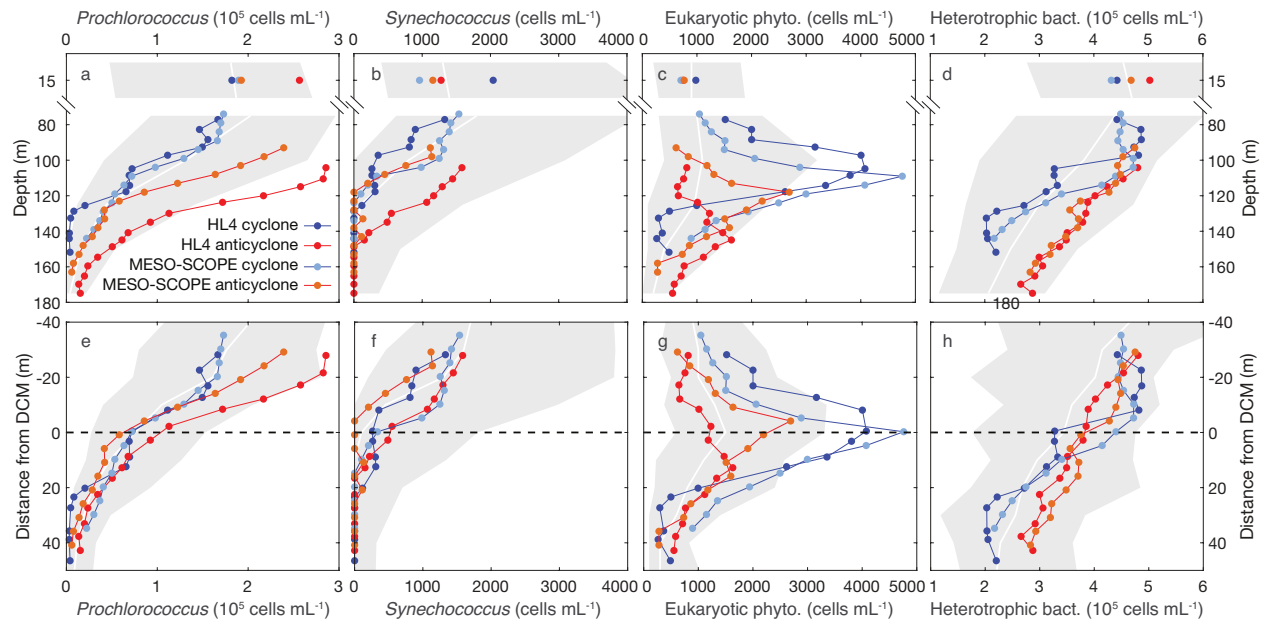
484 *3.4 Mesoscale variability in plankton biomass and community composition*

485 Several consistent patterns in the near-surface waters and at the DCM emerged based on
486 various proxy measurements of plankton biomass at the centers of both pairs of cyclones and
487 anticyclones. In the near-surface waters, there were no apparent eddy-specific differences in
488 concentrations of PC or beam attenuation, nor in chlorophyll *a* concentrations or fluorescence
489 (Figure 7). In contrast, at the depth of the DCM, all of these proxy measurements of plankton
490 biomass were elevated in the cyclonic eddies relative to the anticyclones. The concentration of
491 PC was greater in the DCM of the cyclones relative to anticyclones by 1.3- and 1.4-fold, in the
492 two expeditions (Figure 7a). Similarly, the concentration of chlorophyll *a* was greater in the
493 DCM of the cyclones relative to anticyclones by 1.2- and 1.3-fold (Figure 7c). This difference was
494 even more pronounced for in situ chlorophyll fluorescence (Figure 7d), which includes
495 contributions from pigments other than chlorophyll *a* and can be influenced by variation in
496 fluorescence yield (Roesler et al., 2017). Fluorescence in the DCM was 1.3- and 1.8-fold greater
497 in the cyclonic eddies than in the anticyclones (Figure 7d). Similarly, beam attenuation, an optical
498 proxy for particle concentrations, was 1.4- and 1.5-fold greater at the depth of DCM in the
499 cyclonic eddies relative to the anticyclones (Figure 7b) suggesting enhancement of plankton
500 biomass rather than photoacclimation as drivers of these signals.

501



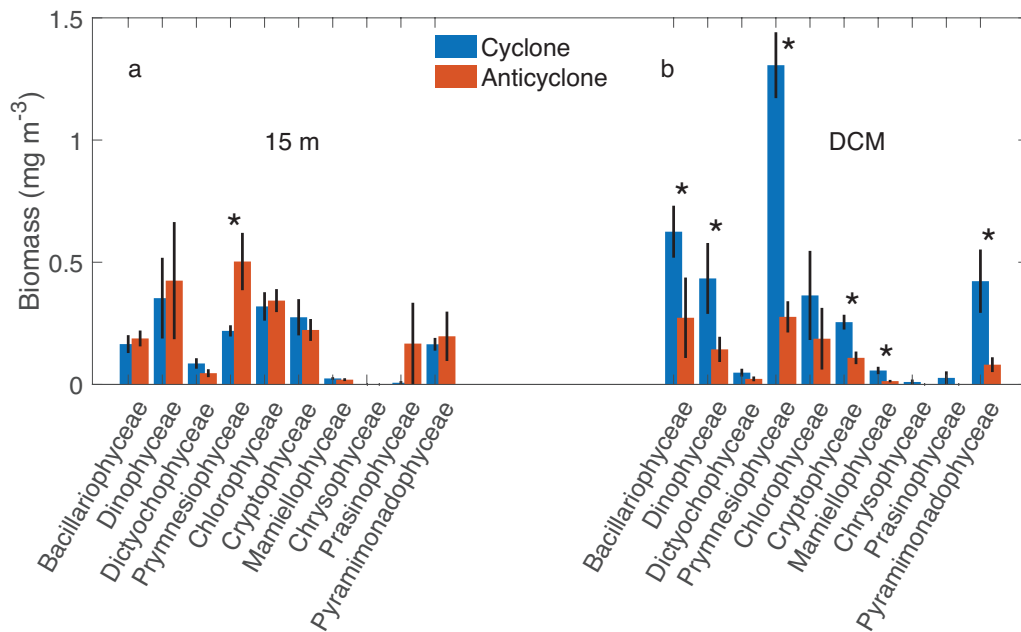
502
 503 **Figure 7:** Average particle and pigment concentrations at 15 m and at the depth of the DCM in the centers of the
 504 cyclones (blue) and anticyclones (red) sampled as part of this study. Panels a) and b) depict the concentrations of PC
 505 and in situ optical measurements of beam attenuation, respectively. Panels c) and d) depict the concentration of
 506 chlorophyll *a* (Chl. *a*) and in situ optical measurements of chlorophyll fluorescence, respectively. Data points in
 507 panels b) and d) were isolated from the same deployments and depths used in samples a) and c). Black lines depict
 508 ± 1 standard deviation of the mean, and are absent when only 1 measurement was available. The top 4 bars depict
 509 observations from 15 m, while the bottom 4 bars depict observations from the DCM. For the HOE-Legacy 4 cruise,
 510 the concentrations of PC and chlorophyll *a* at 15 m were obtained by averaging measurements collected at 5 and 25
 511 m. For the MESO-SCOPE cruise, measurements associated with the Lagrangian sampling periods were used.



512
 513 **Figure 8:** Average abundances of *Prochlorococcus*, *Synechococcus*, eukaryotic phytoplankton, and heterotrophic
 514 bacteria in the centers of the adjacent eddies derived from flow cytometry. Panels a-d) depict vertical profiles of cell
 515 abundances at depths bracketing the DCM in each eddy; the mean cell abundances measured at 15 m are also shown.
 516 Panels e-h) depict the same profiles shown in panels a-d), but the vertical axes are scaled relative to the depth of the
 517 DCM (positive values are deeper). White lines depict the median and shaded areas are the 5th and 95th percentiles of

518 HOT program measurements of these abundances. For the HOE-Legacy 4 cruise, abundances at 15 m were
 519 calculated as the average of measurements at 5 and 25 m. For the MESO-SCOPE cruise, abundances are averaged
 520 from sample collections during the Lagrangian sampling periods.

521 We also evaluated the abundances of *Prochlorococcus*, *Synechococcus*, eukaryotic
 522 phytoplankton, and heterotrophic bacteria in the adjacent eddy pairs based on flow cytometric
 523 analyses. We found that *Prochlorococcus* abundances were greater in the waters above the DCM
 524 in both anticyclones, relative to the cyclones, and relative to the HOT program climatology
 525 (Figure 8a,e). In contrast, eukaryotic phytoplankton (restricted to pico- and nanoplankton)
 526 abundance was elevated in a broad layer near the DCM. Maximum abundance in this layer
 527 exceeded the 95th percentile of HOT observations, with abundances in these eddies >4000 cells
 528 mL⁻¹ (Figure 8c,g). Eukaryotic phytoplankton abundances in the near-surface waters were similar
 529 among the sampled eddies. Vertical distributions of *Synechococcus* were similar among the
 530 sampled eddies and similar to the HOT program observations of this genus (Figure 8b,f).
 531 Heterotrophic bacteria were more abundant in anticyclones than in cyclones in the near-surface
 532 and in waters below the DCM, but this pattern was reversed at depths just above the DCM.



533

534 **Figure 9:** Mean biomass of nano- and microplanktonic (4-100 μm diameter) phytoplankton cells in the (a) near-
535 surface ocean and (b) at the depth of the DCM at the cyclone (blue bars) and anticyclone (red bars) centers sampled
536 during the MESO-SCOPE cruise. Bars depict mean of 7-8 discrete samples collected over 1 day and error bars are \pm
537 1 standard error of the mean. Asterisks depict significant differences in biomass between cyclones and anticyclones
538 (Wilcoxon rank sum test $p < 0.05$).

539 During the MESO-SCOPE cruise, we also examined eddy-driven variability in the biomass
540 of larger eukaryotic phytoplankton cells (4-100 μm in equivalent spherical diameter) imaged with
541 an IFCb. In the near-surface waters, biomass estimates of most of the enumerated phytoplankton
542 were similar between the eddies, with the exception of significantly greater biomass of
543 Prymnesiophyceae in the anticyclone (Figure 8, Wilcoxon rank sum test $p < 0.05$). Conversely, at
544 the depth of the DCM, most phytoplankton classes demonstrated greater biomass in the cyclone
545 than in the anticyclone (Figure 9). The dominant classes in the DCM of the cyclone were
546 Prymnesiophyceae and Bacillariophyceae (specifically members of diatoms), whose biomass was
547 2.3 and 4.7 times greater than in the anticyclone, respectively (Figure 9b). Prymnesiophyceae
548 genera, whose biomass was significantly larger in the DCM of the cyclone compared to the
549 anticyclone (Wilcoxon rank sum test $p < 0.05$), included *Phaeocystis*, *Ophiaster*, *Umbellosphaera*,
550 *Acanthoica*, *Gephyrocapsa*, and *Syracosphaera* (in descending order of average biomass). The
551 Bacillariophyceae genera enriched in the DCM of the cyclone were *Pseudo-nitzschia*,
552 *Chaetoceros*, *Cylindrotheca*, and *Navicula*. Members of the Prymnesiophyceae and
553 Bacillariophyceae are important controls on the formation of calcium carbonate and opal,
554 respectively.

555 3.5 Mesoscale variability in particle export

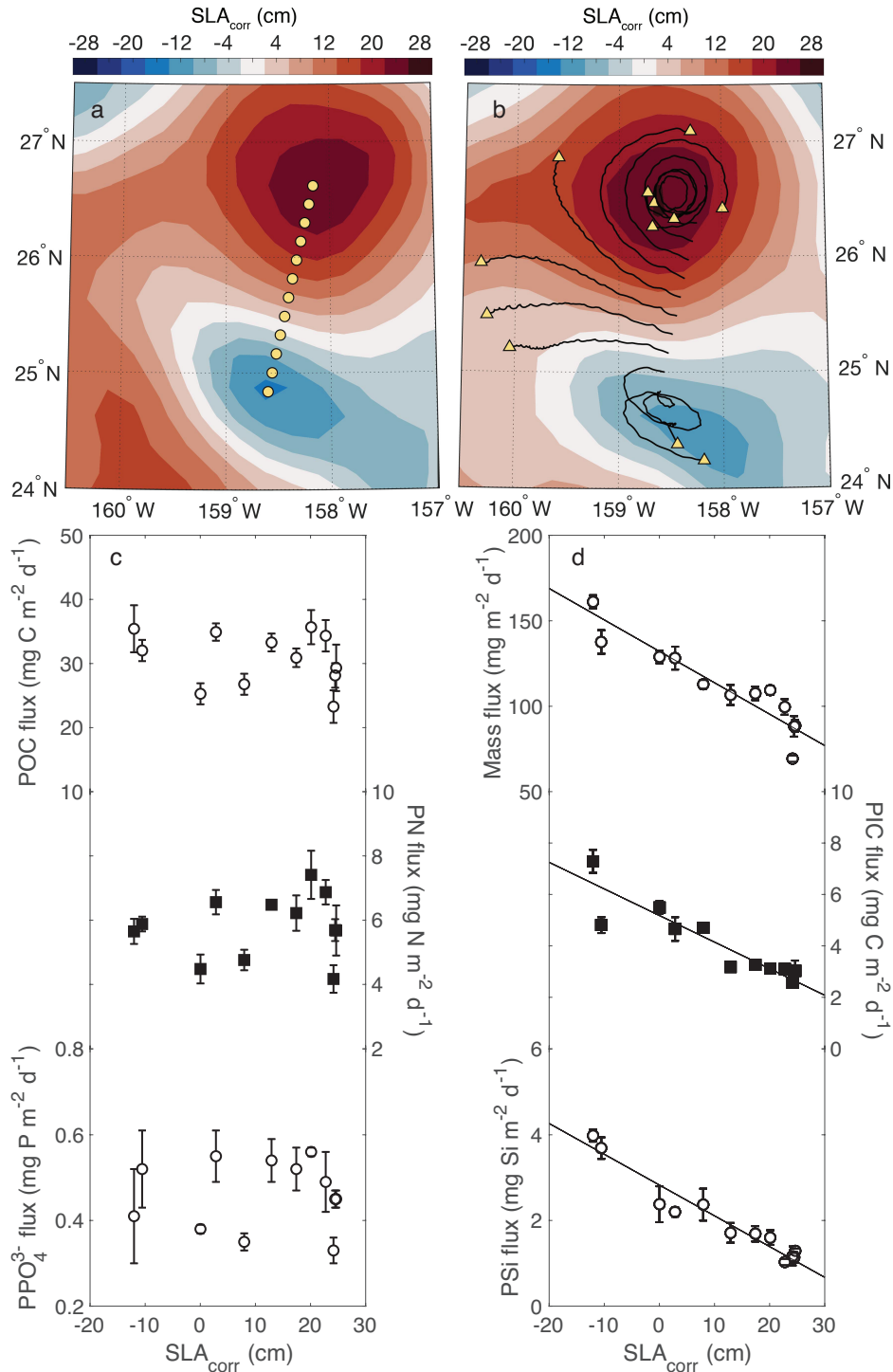
556 Drift tracks of the sediment trap arrays were consistent with geostrophic circulation of the
557 two eddies sampled during MESO-SCOPE (Figure 10a,b). The resulting particle fluxes measured
558 across the adjacent eddies revealed clear mesoscale structure in both the magnitude and

559 stoichiometry of exported particulate matter export. Most notably, despite similarities in POC,
560 PN, and PPO_4^{3-} fluxes across the eddies, total mass, PSi, and PIC export were approximately 2-,
561 4-, and 2.9-fold greater, respectively, in the cyclone relative to the anticyclone (Figure 10c,d;
562 Supplementary Table S1). Moreover, total mass, PSi, and PIC fluxes were all inversely related to
563 SLA_{corr} (Figure 10c,d; Supplementary Table S1). In contrast, fluxes of POC, PN, and PPO_4^{3-} did
564 not vary significantly with spatial variations in SLA_{corr} (Figure 10; Supplementary Table S1;
565 Model II least-squares linear regressions, $p > 0.05$). In the cyclone, export of PIC accounted for
566 17% of the PC flux, with PIC comprising a lower fraction (~10%) of PC flux in the anticyclone
567 (Table 1). The proportions of PIC and PSi to mass flux were inversely related to spatial changes
568 in SLA_{corr} , with PIC:mass flux ratios (g CaCO_3 :g total mass) decreasing from 38% to 28%, and
569 PSi:mass flux ratios (g Si:g total mass) varying from 2.5% to 1.4% across the cyclone to
570 anticyclone transect (Table 1). Because of the proportionally greater contribution of PIC and PSi
571 to mass flux in the cyclonic eddy, POC to mass flux (g C:g total mass) was positively related to
572 SLA_{corr} , with POC representing upwards of 34% of mass flux in the anticyclone and only ~22%
573 in the cyclone (Table 1). In addition to evaluating mesoscale spatial variation in fluxes of key
574 bioelements, we also quantified changes in $\delta^{15}\text{N}$ -PN. The $\delta^{15}\text{N}$ -PN of exported particles was
575 inversely related to changes in SLA_{corr} across the dipole, with the cyclone exporting PN with a
576 $\delta^{15}\text{N}$ signature as great as ~4.3‰, decreasing to as low as 3.0‰ in the anticyclone (Table 1).

577 The elevated contributions of PSi and PIC to particle export in the cyclonic eddy resulted in
578 significant spatial differences in the elemental stoichiometry of particulate matter export across
579 the mesoscale field. Elevated PSi flux in the cyclone coincided with decreasing POC:PSi,
580 PN:PSi, and PPO_4^{3-} :PSi ratios (mol:mol) across the eddies (Table 1). Moreover, all three ratios
581 were positively correlated to changes in SLA_{corr} . Elevated fluxes of PIC within the cyclonic eddy

582 resulted in decreasing PC:PIC, PN:PIC, and PPO_4^{3-} :PIC ratios across the cyclone to anticyclone
583 transect, with all three ratios inversely related to spatial changes in SLA_{corr} (Table 1). In contrast,
584 POC: PPO_4^{3-} and PN: PPO_4^{3-} ratios (mol:mol) did not vary with SLA_{corr} , averaging $173 (\pm 20)$ and
585 $28 (\pm 2.0)$, respectively. Intriguingly, although neither POC nor PN fluxes varied significantly
586 with SLA_{corr} , the ratio of POC:PN was inversely and significantly related to SLA_{corr} (Table 1).

587 Once again, we leveraged HOT program observations to evaluate the generality of the
588 mesoscale variability of particle fluxes across eddies. In this instance, we assessed the
589 significance and strength of the Pearson correlations between HOT particle fluxes and SLA_{corr} .
590 Consistent with our sampling during MESO-SCOPE, we find a lack of correlation between
591 SLA_{corr} and sinking fluxes of PC, PN, and PPO_4^{3-} , but significant negative correlations in fluxes
592 of both P_{Si} and PIC and SLA_{corr} (Supplementary Table S1; $p < 0.05$). While the negative
593 correlations of P_{Si} and PIC are consistent with observations during MESO-SCOPE, we also
594 found a significant positive correlation for HOT observations between $\delta^{15}\text{N}$ and SLA_{corr}
595 (correlation coefficient of 0.14; $p < 0.05$), which was opposite in sign of the relationship observed
596 based on the MESO-SCOPE sediment trap collections.



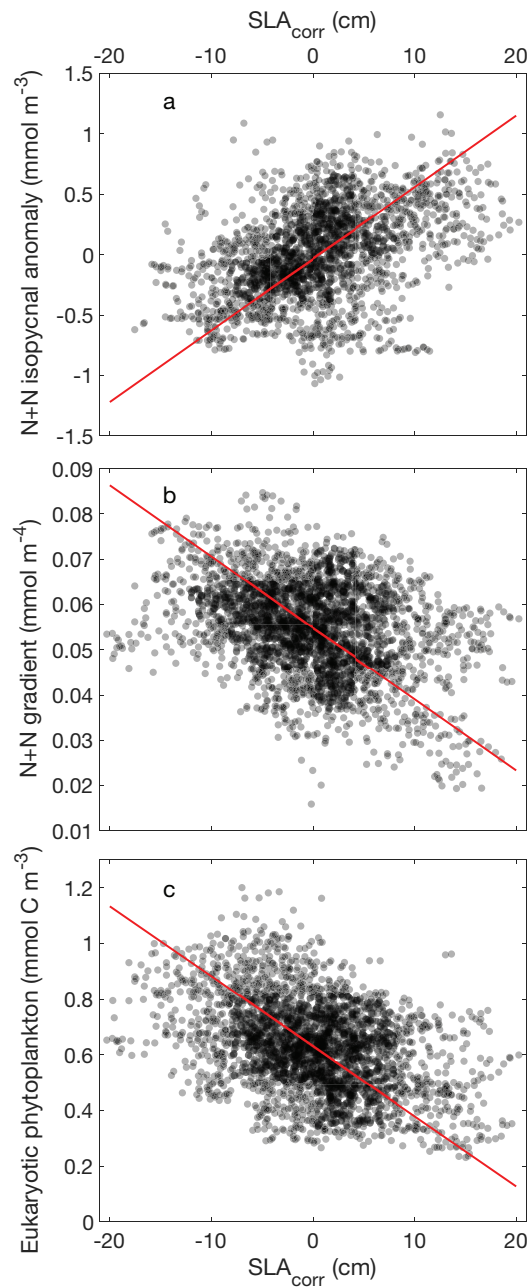
597
 598 **Figure 10:** Results from sediment trap array deployments during the MESO-SCOPE eddy survey. a) Coordinates of
 599 the 12 individual, free-drifting particle interceptor trap arrays at the time of deployment superimposed on the map of
 600 SLA_{corr} for July 2; b) Spatial drift tracks of the particle interceptor traps deployed during the MESO-SCOPE
 601 expedition superimposed on the map of SLA_{corr} on July 14; c) Variability of the fluxes of POC, PN, and PPO₄³⁻ with
 602 SLA_{corr}; d) Relationships between fluxes of total mass, PIC, and PSi with SLA_{corr}. Lines in d) depict the Model II
 603 linear regressions.

604 *3.6 Numerical simulation of the mesoscale variability at Station ALOHA*

605 We used the results of a four-dimensional numerical simulation at Station ALOHA to
606 investigate if the mesoscale variability observed in the field expeditions and HOT program
607 sampling could be reproduced by ecological dynamics captured with the model. Doing so
608 revealed several intriguing similarities and differences between the model results and the
609 empirical observations. The difference between the median potential density measured during
610 HOT and simulated by the model never exceeded 0.1 kg m^{-3} in the upper 175 meters
611 (Supplementary Figure 1). The simulation and field results converged on vertical association of
612 the DCM and the depth of the nutricline (Supplementary Figure 1). However, the model results
613 underestimated concentrations of chlorophyll *a* and primary production in the upper 100 m, and
614 overestimated nutrient concentrations below 75 m (Supplementary Figure 1). Notably, regression
615 analyses of the depth of the 24.6 kg m^{-3} isopycnal versus SLA_{corr} in the model results revealed a
616 vertical displacement of $3.2 \pm 0.0 \text{ m cm}^{-1}$, a mean value very similar to the field observations
617 derived from the HOT program (Barone et al., 2019).

618 We used the numerical model results to identify three patterns of mesoscale variability that
619 we highlighted from our field observations: 1) changes in the isopycnal nutrient concentration
620 with SLA_{corr} near the depth of the DCM; 2) changes in the steepness of the nutricline with
621 SLA_{corr} ; and 3) changes in the biomass of eukaryotic phytoplankton at the DCM with SLA_{corr} .
622 Results from the simulation were consistent with our observations of an increase in the isopycnal
623 nutrient anomaly with SLA_{corr} (Figure 11a) and of decreases in the vertical nutrient gradients and
624 eukaryotic phytoplankton biomass at the DCM with SLA_{corr} (Figure 11b,c). The change in
625 isopycnal nutrient concentration with SLA_{corr} was $0.059 \pm 0.001 \text{ mmol m}^{-3} \text{ cm}^{-1}$, lower than the
626 value of 0.102 ± 0.008 observed in the HOT program observations. Similarly, the change in the

627 steepness of the nutricline in the model ($-0.0016 \pm 0.0000 \text{ mmol m}^{-3} \text{ cm}^{-1}$) was lower than the
628 change observed during HOT ($-0.0023 \pm 0.0002 \text{ mmol m}^{-3} \text{ cm}^{-1}$). The HOT program does not
629 specifically measure eukaryotic phytoplankton biomass among different size plankton classes;
630 hence, we could not directly compare the model simulation to those of the field observations.



631
632 **Figure 11:** Results from a general circulation model (MITgcm) including a multi-species ecological component
633 (Darwin) extracted at Station ALOHA between 1993 and 2015. Co-variation of SLA_{corr} with: a) monthly anomaly of

634 the concentration of N+N on the 24.5 kg m^{-3} isopycnal after removing the long-term trend (365 days running mean)
635 (slope = $0.059 \pm 0.001 \text{ mmol m}^{-3} \text{ cm}^{-1}$, $r=0.41$, $p=3.4 \cdot 10^{-86}$); b) vertical gradients of N+N concentration near the depth
636 of the DCM (slope = $-0.00157 \pm 0.00003 \text{ mmol m}^{-4} \text{ cm}^{-1}$, $r=0.35$, $p=2.1 \cdot 10^{-80}$); c) eukaryotic phytoplankton biomass at
637 the depth of the DCM (slope = $-0.0251 \pm 0.0005 \text{ mmol C m}^{-3} \text{ cm}^{-1}$, $r=0.41$, $p=5.1 \cdot 10^{-111}$). Solid lines depict the Model
638 II linear regressions.

639 **4. Discussion**

640 *4.1 Mesoscale impacts on the nutricline and on the lower euphotic zone*

641 On two separate research cruises in the subtropical North Pacific Ocean, we sampled pairs
642 of adjacent mesoscale eddies of opposite polarity in late spring and summer, providing an
643 opportunity for comparative analyses of upper ocean biogeochemistry and plankton ecology
644 associated with mesoscale features in close ($<200 \text{ km}$) spatial proximity. Based on these
645 analyses, we identified common features associated with eddies of similar polarity and we then
646 used the time-resolved, Eulerian HOT program observations to evaluate the generality of
647 mesoscale disturbances on the behavior of the upper ocean in this oligotrophic habitat. Notably,
648 our findings suggest that mesoscale motions have a large impact on plankton biogeochemistry in
649 the lower euphotic zone, but such dynamics are not as apparent in the well-lit near-surface ocean.
650 These results are consistent with a previous study that found time-varying mesoscale dynamics
651 structured much of the temporal variability in temperature and nutrient stoichiometry in the
652 dimly-lit lower euphotic zone at Station ALOHA, but had limited influence on these properties
653 through the well-lit upper ocean (Church et al. 2009). In the current study, by coupling our
654 sampling of adjacent eddies with a multi-decadal analysis of HOT program observations, we find
655 robust differences between cyclones and anticyclones in concentrations of chlorophyll *a*,
656 dissolved O_2 , inorganic nutrients, and particle load in the lower euphotic zone. However,
657 differences in these properties were not apparent in the well-lit upper ocean waters.

658 The consistent biogeochemical responses to mesoscale motions observed in the lower
659 euphotic zone reflect rapid plankton assimilation of nutrients with concomitant increases in
660 eukaryotic phytoplankton biomass, as the nutricline undergoes mesoscale-driven oscillations
661 across the exponentially varying light field. This variability in the lower euphotic zone is
662 consistent with previous findings on the change in the vertical distributions of nutrients and
663 biomass related to mesoscale activity at Station ALOHA (Church et al., 2009; Barone et al.,
664 2019). The eddies sampled as part of this study bracketed the full dynamic range of SLA_{corr}
665 variability observed at Station ALOHA and revealed that mesoscale motions can vertically
666 perturb isopycnals in the lower euphotic zone by more than 100 m. The large vertical excursions
667 of isopycnals near the DCM alter the ambient light field by more than an order of magnitude
668 (*e.g.*, during MESO-SCOPE measured light fluxes along the 24.5 kg m^{-3} isopycnal varied 0.11 to
669 $3.4 \text{ moles photon m}^{-2} \text{ d}^{-1}$ between the anticyclone and the cyclone). Such large variations in light
670 intensity would be expected to stimulate phytoplankton production in the light-limited DCM
671 (Goldman 1993; Goldman and McGillicuddy 2003; Li et al. 2011), with concomitant impacts on
672 concentrations of nutrients and dissolved O_2 , a finding consistent with our analyses of historical
673 HOT program observations. The dynamics identified in this study may be a common feature of
674 oligotrophic ocean ecosystems during those periods of the year when the base of the mixed layer
675 remains vertically well separated from the top of the nutricline. This vertical separation, coupled
676 with rapid assimilation of inorganic nutrients by the plankton community in the DCM layer,
677 limits the impact of mesoscale eddies on phytoplankton growing in the well-lit, near-surface
678 oceans.

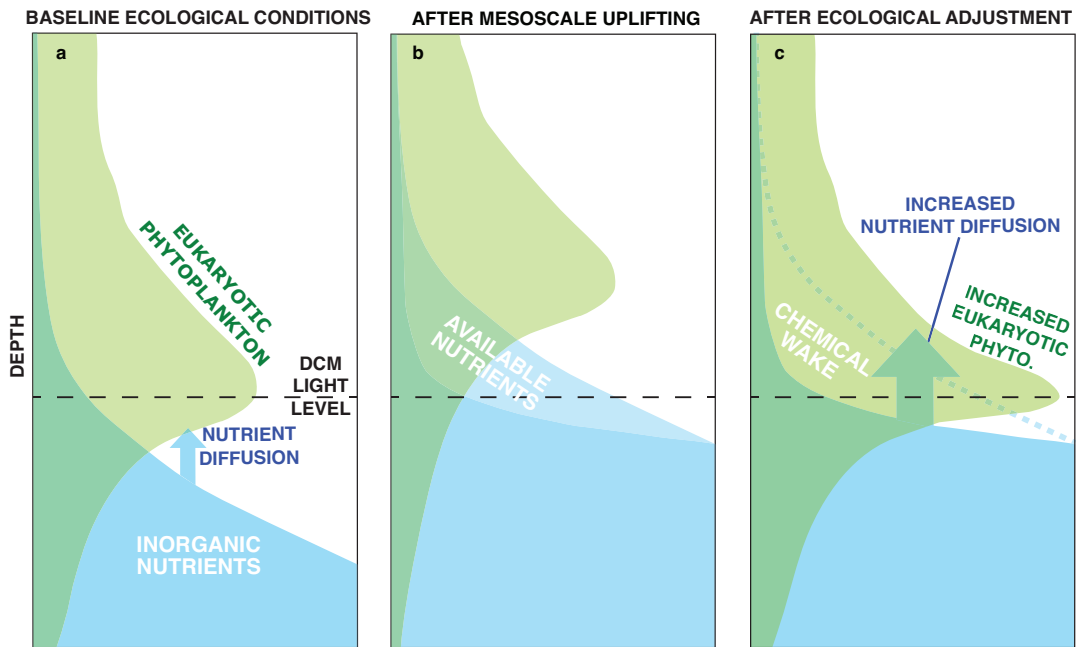
679 It has been previously proposed that the mesoscale stimulation of phytoplankton activity is
680 limited to the intensification stage of cyclonic eddies (Sweeney et al., 2003; Rii et al., 2008). Our

681 observations extend this model: we observed an increase in phytoplankton biomass in the DCM
682 of cyclonic eddies several weeks after their intensification (eddy life cycles in Supplementary
683 information). These observations suggest that mesoscale delivery of inorganic nutrients to the
684 lower euphotic zone is not limited to the active upwelling phase of the eddy life cycle (the
685 intensification stage), but continues well into the mature phase of an eddy. We propose continued
686 nutrient delivery to the lower euphotic zone is maintained late into the lifetime of cyclonic eddies
687 due to the steepening of the vertical nutrient gradients that accompanies vertical uplift of the
688 thermocline and subsequent biological erosion of the top of the nutricline. In subtropical gyres,
689 the DCM is often vertically associated with the top of the nitracline (Herbland and Voituriez,
690 1979; Cullen and Eppley, 1981; Bahamón et al., 2003; Letelier et al., 2004), here defined as the
691 layer where inorganic nitrogen concentrations start increasing with depth, and where turbulent
692 mixing provides an upward flux of inorganic nitrogen to the euphotic zone (Lewis et al., 1986;
693 Anderson, 1969). The vertical positioning of both these features appears structured by light;
694 during isopycnal uplift that accompanies cyclones, light-limited phytoplankton communities are
695 vertically transplanted upward across the exponentially increasing light field, stimulating net
696 productivity (as reflected in increased eukaryotic phytoplankton biomass), producing O₂ and
697 consuming nutrients.

698 Based on analyses of the vertical concentration gradients in inorganic nutrients due to
699 isopycnal heaving, we estimate the role of eddies in driving diapycnal fluxes of inorganic
700 nutrients into the euphotic zone. This analysis assumes that changes in the first vertical derivative
701 in nutrient concentrations are not counterbalanced by opposite changes in diapycnal eddy
702 diffusivity. Under this assumption, we find that vertical displacement of the nutricline associated

703 with cyclones increases net diapycnal fluxes of N+N and PO₄³⁻ by upwards of 9-fold and 11-fold,
704 respectively, relative to anticyclones (Figure 6).

705 To explain our observations, we propose a conceptual framework that describes the temporal
706 dynamics associated with cyclonic uplift of the nutricline in the stratified ocean (Figure 12). Prior
707 to the intensification of the cyclonic eddy, the biomass maximum of eukaryotic phytoplankton
708 coincides with the DCM, at a depth determined by the downward light flux (Figure 12a; Letelier
709 et al., 2004). Mesoscale uplift results in upward displacement of the DCM community and the
710 nutricline, increasing light in layers where its flux otherwise limits phytoplankton growth (Figure
711 12b). As a response to this uplift, phytoplankton utilize the additional light energy available,
712 increasing in biomass and consuming the available nutrients. This upward isopycnal
713 displacement drives increases in net photosynthetic production, and over time results in a
714 "chemical wake," observed as a negative nutrient anomaly (Figure 12c) and a positive O₂
715 anomaly in the waters above the DCM. One important consequence of nutrient removal by this
716 mechanism is a steepening of the nutricline and presumed intensification of diapycnal nutrient
717 fluxes, maintaining elevated eukaryotic phytoplankton biomass within the DCM (Figure 12c),
718 which now lies within denser waters.



719
 720 **Figure 12:** Ecological plankton dynamics in a mesoscale cyclone during three idealized steps: a) before the cyclone
 721 origin; b) after an instantaneous uplifting caused by eddy intensification; and c) after the ecosystem responds to the
 722 uplifting and a new DCM community emerges and consumes the inorganic nutrients made available by the uplifting
 723 of the nutricline.

724
 725 The simplified conceptual framework depicted in Figure 12 synthesizes our view of
 726 biogeochemical dynamics associated with the uplift of the thermocline in cyclones, where
 727 increased nutrient delivery to the lower euphotic zone continues after the eddy intensification
 728 phase, a finding we attribute to increased vertical nutrient gradients. A link between SLA_{corr} and
 729 diapycnal nutrient fluxes had been previously noticed by Barone et al. (2019), but this study
 730 provides additional support that mature phase cyclonic eddies can continue to support
 731 phytoplankton production. We propose that net phytoplankton growth during eddy intensification
 732 erodes the top of the nutricline, evident in our study as a negative isopycnal anomaly of nutrient
 733 concentrations, which in turn increases diapycnal fluxes of nutrients into the lower euphotic zone
 734 during the mature phases of cyclonic eddies. We also utilized a four-dimensional numerical

735 model to investigate if the variability observed in our empirical observations were captured by a
736 dynamic ecosystem model, where light and nutrient limitation regulate phytoplankton growth
737 (Dutkiewicz et al., 2015). Analyses of the model results from Station ALOHA further supports
738 our conceptual framework linking erosion of the nutricline to diapycnal nutrient fluxes and
739 increased biomass of eukaryotic phytoplankton near the DCM during periods of low SLA_{corr} .
740 These results reinforce our conclusion that mesoscale oscillations of the thermocline coupled
741 with simple ecological dynamics lead to a modification of the characteristics of the lower
742 euphotic zone that extends the ecological impact of cyclonic eddies beyond their intensification
743 phase.

744

745 *4.2 Mesoscale alterations in O_2 and nutrient stoichiometry*

746 Our analyses on the biogeochemical variability along isopycnal surfaces showed that mesoscale
747 dynamics vertically decouple O_2 production from nutrient consumption. As an example, during
748 the MESO-SCOPE cruise, the 24.5 kg m^{-3} isopycnal was displaced upwards to a depth of 64 m in
749 the center of the cyclonic eddy, which was 65 m shallower relative to the position of the same
750 isopycnal in the anticyclone. This displacement increased the daily light flux to this isopycnal in
751 the cyclone by more than an order of magnitude relative to the mean light flux measured in the
752 center of the anticyclone ($3.4 \text{ mol photons m}^{-2} \text{ d}^{-1}$ versus $0.11 \text{ mol photons m}^{-2} \text{ d}^{-1}$). The increased
753 light presumably stimulated net community production, which was linked with an excess 23
754 $\text{mmol } O_2 \text{ m}^{-3}$ measured on the 24.5 kg m^{-3} isopycnal in the center of the cyclone with respect to
755 the average concentration measured during the eddy survey on the same isopycnal. Similarly,
756 inorganic nutrient consumption resulted in isopycnal concentration anomalies of $N+N$ and PO_4^{3-}
757 of $-0.21 \text{ mmol N m}^{-3}$ and $-0.043 \text{ mmol P m}^{-3}$, respectively. The resulting $O_2:N$ and $O_2:P$ molar

758 stoichiometries (110:1 and 535:1, respectively) suggested excess net O₂ production with respect
759 to the consumption of inorganic nutrients. This phenomenon was widespread in both cyclone
760 centers, where it was observed in a depth layer above the DCM approximately between 50 and
761 100 m, with an excess of O₂ with respect to N+N reaching values above 10 mmol m⁻³ (Figure 5).
762 Conversely, below 100 m, all eddy centers were characterized by a deficit in O₂ with respect to
763 the concentration expected based on inorganic nutrient concentrations (Figure 5). The
764 observation of similar variability in eddies of opposite polarity is intriguing considering the
765 isopycnal anomalies must sum to zero across each eddy transect, but it is possible that different
766 mechanisms produced the O₂ deficits in cyclones and anticyclones.

767 A number of previous studies, including several based at Station ALOHA, have reported
768 anomalous O₂ to nutrient stoichiometries similar to those described in this study. Using apparent
769 oxygen utilization (AOU; defined as O₂ solubility – O₂ measured) as a measure of the cumulative
770 respiratory consumption of O₂ that has occurred since a water parcel last ventilated with the
771 atmosphere, and assuming fixed stoichiometry between respiratory O₂ consumption and N
772 regenerated through mineralization, Emerson and Hayward (1995) found that O₂:N
773 stoichiometries deviated substantially from those expected based on Redfield mineralization of
774 organic matter in the lower euphotic zone and upper mesopelagic waters. More recently,
775 leveraging autonomous profiling floats equipped with O₂ and NO₃⁻ sensors, Johnson et al. (2010)
776 documented consistent supersaturation of O₂ in the well-lit euphotic zone waters and an apparent
777 deficit of NO₃⁻ (relative to respiratory O₂ consumption) at depth. Moreover, these authors found
778 that the “overproduction” of O₂ relative to NO₃⁻ consumed in the upper euphotic zone could be
779 balanced by the NO₃⁻ consumption without corresponding O₂ production at depth (Johnson et al.
780 2010). In a subsequent analysis of profiling float O₂ and NO₃⁻ data from the subtropical North

781 Pacific, Ascani et al. (2013) identified discrete stoichiometric “regimes”, differentiated by the
782 vertical position of the isopycnal surface. Similar to the current study, along isopycnal surfaces
783 typically confined to the upper euphotic zone, where nutrient concentrations were minimal, O₂
784 concentrations increased independent of measurable changes in NO₃⁻ (Ascani et al., 2013). In
785 contrast, O₂ and NO₃⁻ generally co-varied in near-Redfield proportions along isopycnals located
786 in the dimly-lit or dark waters of the upper ocean (Ascani et al., 2013).

787 Several mechanisms have been proposed as underlying the formation of anomalous ratios
788 in the concentration of O₂ and inorganic nutrients. Emerson and Hayward (1995) argue that
789 mineralization of dissolved organic matter that is substantially enriched in C relative to N and P
790 likely underlies the formation of anomalous O₂:N stoichiometries. A subsequent study by Abell
791 et al. (2005) used an along-isopycnal mass balance model to quantify mineralization of DOM as a
792 mechanism maintaining the anomalous stoichiometry observed in the lower euphotic zone,
793 concluding that mineralization of C-enriched DOM (i.e., C:N molar ratio of 30-32) could explain
794 the anomalous O₂ and nutrient stoichiometry. Similarly, Fawcett et al. (2018) argued that
795 production of C-rich organic matter in the well-lit euphotic zone, and subsequent consumption of
796 that material at depth, together with heterotrophic bacterial assimilation of NO₃⁻, resulted in the
797 anomalous O₂ to nutrient stoichiometry observed in the Sargasso Sea. More recently, using
798 measurements from Station ALOHA, Letscher and Villareal (2018) argued additional processes,
799 namely phytoplankton vertical migration, must also be invoked to explain the apparent O₂ to
800 nutrient imbalance. Formation of nitrous oxide during nitrogen oxidation (e.g., ammonia or NO₂⁻
801 oxidation) that occurs in the lower euphotic zone and upper mesopelagic waters would further
802 alter the stoichiometry of O₂ consumed relative to NO₃⁻ produced (Wilson et al. 2014). Based on
803 our eddy-centric observations, it appears different mechanisms may be best suited to explain the

804 anomalies in anticyclones and in cyclones. In anticyclones, the subduction of near-surface water
805 could provide high concentrations of C-rich organic matter to the lower euphotic zone, which
806 would be later mineralized and result in lower O₂ concentrations relative to concentrations of
807 inorganic nutrients that would be produced if the organic matter were mineralized in typical (i.e.,
808 Redfieldian) stoichiometry. Conversely, vertically-migrating phytoplankton might consume
809 nutrients near the top of the nutricline and actively move upward to photosynthesize (Villareal et
810 al. 1993), which could explain both the O₂ deficit below 100 m (where nutrients are taken up
811 without O₂ production) and the O₂ surplus in the 50-100 m layer (where O₂ is produced without
812 nutrient uptake) in the cyclonic eddies.

813

814 *4.3 Mesoscale variability in particle fluxes*

815 By deploying a suite of 12 individual, drifting sediment trap arrays across two adjacent eddies
816 of opposite polarities we obtained spatially-resolved information on particle export across a large
817 mesoscale gradient (SLA_{corr} for these deployments ranged between -12 cm to 25 cm). Although
818 export of organic matter (POC, PN, and PPO₄) was similar across and within this mesoscale
819 gradient, total mass flux varied more than 2-fold, coincident with approximately 4-fold changes
820 in export of P_{Si} and P_{IC}. Export of total mass, P_{Si}, and P_{IC} were all greatest in the cyclone
821 center (lowest SLA_{corr}) and decreased linearly with increases in SLA_{corr}. Moreover, the δ¹⁵N
822 signature of sinking PN points to differing sources of N supporting export across these eddies.
823 While these observations were collected in strong mesoscale eddies, they depict several patterns
824 of particle flux variability broadly linked with different classes of mesoscale motions, as
825 demonstrated by the analysis of historical observations from the HOT program. Consistent with
826 measurements in MESO-SCOPE, the HOT particle fluxes of P_C, P_N, and PPO₄ were not

827 significantly correlated with SLA_{corr} , a finding previously reported by Barone et al. (2019), while
828 a negative correlation was observed for PIC and P*S*i. Conversely, the increased $\delta^{15}PN$ in the
829 MESO-SCOPE cyclone is in the opposite direction of the HOT positive correlation of $\delta^{15}PN$ and
830 SLA_{corr} .

831 To put our observations into context, it has been previously proposed that the upwelling of
832 nutrient-rich water during the intensification of cyclonic eddies is a major cause of mesoscale
833 variability in particle fluxes (Sweeney et al., 2003; Rii et al., 2008). However, we believe that our
834 observations are not directly linked to this process, for two main reasons: 1) the correlations of
835 particle fluxes with SLA_{corr} point to a connection with the depth of the thermocline rather than
836 with the vertical velocities that would be associated with eddy intensification or weakening; and
837 2) the cyclone sampled during MESO-SCOPE had its nearest intensification event 32 days before
838 our sampling (Supplementary information). As a consequence, we postulate that the mesoscale
839 variation detected in our measurements is a product of the shallower and steeper nutricline at low
840 SLA_{corr} , which sustains a more abundant population of eukaryotic phytoplankton, including
841 diatoms and prymnesiophytes, with subsequent impact on the export of biomineralized particles.
842 In contrast, the deeper nutricline in anticyclonic eddies appears to favor the proliferation of small
843 picoplanktonic cyanobacteria (i.e., *Prochlorococcus*; Barone et al. 2019). The MESO-SCOPE
844 anticyclonic eddy also contained nearly twice the concentration of dissolved iron than is typically
845 found at the DCM at Station ALOHA, which may have supported the increase in
846 *Prochlorococcus* abundance near the DCM (Hawco et al., companion submission).

847 One of the most striking observations from the MESO-SCOPE sediment trap deployments
848 were the robust inverse relationships between SLA_{corr} and P*S*i, PIC, and total mass flux.
849 Enhanced P*S*i export has been previously reported for a wind-driven cyclone south of the

850 Hawaiian archipelago (Benitez-Nelson et al., 2007; Rii et al., 2008); however, our observations
851 provide evidence that cyclonic eddies may also promote PIC export. To our knowledge, these are
852 the first observations linking export of PIC to mesoscale dynamics. The enhanced fluxes of P*S*i
853 and PIC observed during MESO-SCOPE provides some insights into the phytoplankton likely
854 fueling particle export in the cyclone, specifically diatoms and prymnesiophytes, whose biomass
855 was elevated in the DCM of the cyclone relative to the DCM of the anticyclone. Diatoms and
856 prymnesiophytes are key phytoplankton taxa containing opal and calcium carbonate, but some
857 large zooplankton of the group Rhizaria also have mineral skeletons of calcium carbonate (e.g.,
858 Foraminifera) or opal (e.g., Radiolaria). We could not quantify the abundance of large Rhizaria
859 (>100µm in diameter) with the methods employed in this study so we cannot exclude
860 contributions from these organisms to the observed variations in the export of P*S*i and PIC
861 between eddies of different polarity. A number of previous studies have identified elevated
862 diatom and prymnesiophyte biomass in the DCM of cyclonic eddies (Bidigare et al., 2003;
863 Benitez-Nelson et al. 2007; Rii et al., 2008). In a microscopy-based assessment of diatoms,
864 Scharek et al. (1999) found low contributions to sinking particle export by members of the DCM
865 diatom assemblage, but they noted how a substantial fraction of the diatom frustules were empty
866 (lacking cytoplasm). Similarly, Benitez-Nelson et al. (2009) concluded that coupling between
867 phytoplankton growth and microzooplankton grazing in Hawaiian lee cyclones resulted in export
868 of empty diatom frustules, thereby increasing the P*S*i:POC ratio of the trap-derived material.
869 Based on pigment and gene-based analyses, Li et al. (2013) concluded that diatoms and
870 prymnesiophytes comprised approximately 2% and 20%, respectively, of total chlorophyll *a* in
871 the lower euphotic zone at Station ALOHA. However, the proportion of diatom and
872 prymnesiophyte genes exported, relative to the euphotic zone inventory, averaged 0.15% d⁻¹ and

873 0.19% d⁻¹, compared to the 5% d⁻¹ P_{Si} export : inventory (Li et al., 2013). These results appear
874 consistent with the interpretation that empty diatom frustules and calcified liths underlie the
875 elevated P_{Si} and PIC fluxes in the MESO-SCOPE cyclone.

876 In addition to clear relationships between mass, P_{Si}, and PIC fluxes, the δ¹⁵N of the exported
877 PN demonstrated a significant inverse relationship to SLA_{corr} during MESO-SCOPE (i.e., the
878 δ¹⁵N of PN was more enriched in the cyclone relative to the anticyclone). A number of previous
879 studies have utilized a two-end member isotope model, leveraging differences in the δ¹⁵N
880 signatures of deep water NO₃⁻ and N₂, to estimate the proportion of PN export supported by NO₃⁻
881 assimilation and N₂ fixation at Station ALOHA (Karl et al., 1997; Dore et al., 2002; Casciotti et
882 al., 2008; Böttjer et al. 2016). Assuming only two potential sources of N (NO₃⁻ assimilation and
883 N₂ fixation) support PN export, these observations suggest that NO₃⁻ assimilation was relatively
884 more important in the cyclone (where NO₃⁻ appeared to support upwards of 85% of PN export)
885 while N₂ fixation was relatively more important in the anticyclone (where N₂ fixation was
886 estimated to support upwards of 40% of PN export). While it would be tempting to attribute the
887 δ¹⁵N variability to changes in the diapycnal fluxes of NO₃⁻ linked with changes in the steepness
888 of the nutricline, this is probably not the case: Based on the observations from the HOT program,
889 we found steepening of the nutricline with decreasing SLA_{corr}, but a positive correlation between
890 δ¹⁵N and SLA_{corr}, opposite in sign to the variation observed during MESO-SCOPE. Since
891 diapycnal fluxes were likely not driving the change in δ¹⁵N across eddies, this variation might
892 have been supported by high rates of N₂ fixation by the abundant diazotroph *Crocospaera*
893 measured in the MESO-SCOPE anticyclone (Dugenne et al., 2020). A number of previous
894 studies have documented increases in N₂ fixation and N₂-fixing microorganism biomass
895 associated with anticyclonic eddies (Davis and McGullicuddy, 2006; Fong et al., 2008; Wilson et

896 al., 2017). During the warm summer months (June-October), rates of N₂ fixation at Station
897 ALOHA often peak during periods of positive SLA_{corr} such as those associated with anticyclones
898 (Church et al., 2009; Böttjer et al., 2016). The gradient in δ¹⁵N of PN export across the mesoscale
899 eddies sampled in the current study further reinforce the apparent promotion of N₂ fixation in
900 anticyclones during the summer.

901 In the NPSG, the mesoscale delivery of inorganic nutrients to the euphotic zone through
902 upwelling is larger than the delivery caused by changes in diapycnal mixing (Barone et al., 2019).
903 While we think that upwelling was not responsible for the variability in particle fluxes across
904 eddies observed in this study, its effect is clearly evident in the positive isopycnal anomalies of
905 O₂ and negative isopycnal anomalies of inorganic nutrients measured in cyclones. So what was
906 the fate of the POC, PN, and PPO₄ synthesized to produce the isopycnal O₂ anomalies before we
907 sampled the eddies? During HL4 and MESO-SCOPE, 50-200 m depth integrated O₂ saturation
908 anomalies (taking into account changes in solubility) in the cyclone centers were 2152 mmol O₂
909 m⁻² and 772 mmol O₂ m⁻², respectively, suggesting excess O₂ produced in the lower euphotic
910 zone was not accompanied by concomitant consumption of O₂ via respiration of organic matter in
911 the top of the mesopelagic zone. Suspended PC inventories during HL4 and MESO-SCOPE
912 appear too low to account for the formation of O₂ isopycnal anomalies. Furthermore, we did not
913 measure dissolved organic carbon, but concentrations of dissolved organic N and P were lower in
914 the cyclone than in the anticyclones (data not shown). Such findings suggest that the organic
915 matter produced which resulted in the cyclone O₂ anomalies likely was no longer in the dissolved
916 and particulate stocks in the upper ocean, but rather had already been exported to deeper waters,
917 presumably through particle settling or through the action of vertically migrating zooplankton. As
918 a consequence, the biogeochemical signatures associated with nutrient consumption and O₂

919 production remained in the euphotic zone as a “chemical wake”, reflecting the prior history of
920 productivity and export associated with cyclonic uplift of the isopycnal surfaces. Taken together,
921 the isopycnal anomalies and sediment trap fluxes indicate that the MESO-SCOPE cruise likely
922 sampled the cyclonic eddy at some point after the peak period of organic matter export, and that
923 the P*S*i and P*C* export patterns reflected settling of empty diatom frustules and calcified liths
924 from the DCM phytoplankton community, which was sustained by the enhanced diapycnal
925 nutrient fluxes during the mature stage of the eddy.

926

927 **5. Conclusions**

928 By sampling adjacent eddies of opposite polarity we identified several impacts of mesoscale
929 motions on plankton biology and upper ocean biogeochemistry in the subtropical North Pacific
930 Ocean. Some key findings that emerged from our study are:

- 931 1. Cyclonic isopycnal uplift increased vertical gradients in inorganic nutrients through the
932 biological erosion of the top of the nutricline. This presumably increased the diapycnal
933 flux of nutrients delivered to the lower euphotic zone and supported increased eukaryotic
934 phytoplankton biomass. Conversely, depression of isopycnals in anticyclones decreased
935 nutrient concentration gradients in the lower euphotic zone, a dynamic that appeared to
936 increase *Prochlorococcus* biomass above the DCM.
- 937 2. Mesoscale changes in inorganic nutrients and dissolved O₂ concentrations are vertically
938 decoupled. For example, upward displacement of isopycnals associated with cyclonic
939 eddies resulted in peak consumption of inorganic nutrients occurring deeper than the layer
940 where O₂ production was maximal. In contrast, both cyclones and anticyclones appeared

941 to have less O₂ than expected based on nutrient concentrations in the layer below the
942 DCM.

943 3. Particle-associated biomineral fluxes of P_{Si} and P_{IC} were inversely related to SLA_{corr}
944 despite no differences in export of POC, PN, and PPO₄³⁻. Elevated biomineral export at
945 low SLA_{corr} presumably reflects increased contributions from silicifying and calcifying
946 plankton consistent with observations of elevated biomass of Bacillariophyceae and
947 Prymnesiophytes in the cyclone DCM. Moreover, the δ¹⁵N of sinking particles revealed
948 differences in N sources supporting production across adjacent eddies, with a larger
949 contribution by N₂ fixation in the anticyclone.

950 Our study highlights the spatiotemporal complexity of ocean ecosystems, and the inherent
951 challenges such complexity presents to Eulerian observations such as the HOT program. Across a
952 region of the ocean stretching a few hundreds of kilometers, the presence of strong, mature,
953 mesoscale eddies of opposite polarity resulted in striking differences in ocean biogeochemistry.
954 We found eddy-dependent isopycnal displacements through the upper ocean light field alter the
955 steepness of the nutricline, influence the biomass of eukaryotic phytoplankton (including
956 members of the prymnesiophytes and diatoms) and *Prochlorococcus*, and impact the export of
957 opal and carbonate. These observations expand our understanding of the biogeochemical impacts
958 of mesoscale motions by describing the stoichiometry of the erosion of the nutricline in cyclonic
959 eddies and by highlighting a series of cascading dynamics that result from this erosion.

960
961

962 **Acknowledgements**

963 We warmly thank Tara Clemente (University of Hawaii) for her leadership during the HOE-
964 Legacy 4 and MESO-SCOPE expeditions. We are also grateful to Tim Burrell, Eric
965 Shimabukuro, and Ryan Tabata (University of Hawaii) for their tireless efforts during field
966 operations. We are grateful to Joshua Weitz and David Demory (Georgia Institute of
967 Technology) for their thoughtful comments on the manuscript. We thank Susan Curless, Eric
968 Grabowski, and Alexa Nelson (University of Hawaii) for the analysis of inorganic nutrients and
969 sinking particle fluxes. The isotopic composition of nitrogen of sinking particles was done by the
970 Popp lab (University of Hawaii). SLA is available from the Copernicus Marine and Environment
971 Monitoring Service (<http://www.marine.copernicus.eu>). HOT observations are available through
972 HOT-DOGS (<http://hahana.soest.hawaii.edu/hot/hot-dogs/>). Results from the numerical model
973 can be accessed at <https://doi.org/10.6075/J0BR8QJ1>. All other measurements used for the
974 analyses of this manuscript are available at <https://doi.org/10.5281/zenodo.5048504>. This work
975 was supported by grants from the Simons Foundation (# 329108 to DMK, EFD, MJF, MJC,
976 AEW, SGJ; 721252 to DMK; 721223 to EFD; 721221 to MJC; 721256 to AEW; 721250 to SGJ).

977

978
979 **References**

980

981 Abell, J., Emerson, S., and Keil, R. G. (2005). Using preformed nitrate to infer decadal changes
982 in DOM remineralization in the subtropical North Pacific. *Global biogeochemical cycles*, 19(1).
983 <https://doi.org/10.1029/2004GB002285>

984

985 Anderson, G. C. (1969). Subsurface chlorophyll maximum in the Northeast Pacific Ocean.

986 *Limnology and Oceanography*, 14, 386–391. <https://doi.org/10.4319/lo.1969.14.3.0386>

987

988 Anderson, L. A., and Sarmiento, J. L. (1994). Redfield ratios of remineralization determined by
989 nutrient data analysis, *Global Biogeochemical Cycles*, 8(1), 65– 80.
990 <https://doi.org/10.1029/93GB03318>

991

992 Anderson, L. A. (1995). On the hydrogen and oxygen content of marine phytoplankton. *Deep-*
993 *Sea Research Part I: Oceanographic Research Papers*, 42, 1675–1680.
994 [https://doi.org/10.1016/0967-0637\(95\)00072-E](https://doi.org/10.1016/0967-0637(95)00072-E)

995

996 Ascani, F., Richards, K. J., Firing, E., Grant, S., Johnson, K. S., Jia, Y., ... and Karl, D. M.
997 (2013). Physical and biological controls of nitrate concentrations in the upper subtropical North
998 Pacific Ocean. *Deep-Sea Research Part II: Topical Studies in Oceanography*, 93, 119-134.
999 <https://doi.org/10.1016/j.dsr2.2013.01.034>

1000

1001 Bahamón, N., Velasquez, Z., and Cruzado, A. (2003). Chlorophyll *a* and nitrogen flux in the
1002 tropical North Atlantic Ocean. *Deep-Sea Research Part I: Oceanographic Research Papers*,
1003 50(10–11), 1189–1203. [https://doi.org/10.1016/S0967-0637\(03\)00145-6](https://doi.org/10.1016/S0967-0637(03)00145-6)

1004

1005 Barone, B., Coenen, A. R., Beckett, S. J., McGillicuddy, D. J., Weitz, J. S., and Karl, D. M.
1006 (2019). The ecological and biogeochemical state of the North Pacific Subtropical Gyre is linked
1007 to sea surface height. *Journal of Marine Research*, 77(2), 215-245.
1008 <https://doi.org/10.1357/002224019828474241>

1009

1010 Benitez-Nelson, C. R., Bidigare, R. R., Dickey, T. D., Landry, M. R., Leonard, C. L., Brown, S.

1011 L., ... and Yang, E. J. (2007). Mesoscale eddies drive increased silica export in the subtropical
1012 Pacific Ocean. *Science* 316(5827), 1017-1021. <https://doi.org/10.1126/science.1136221>
1013

1014 Bidigare, R. R., Benitez-Nelson, C., Leonard, C. L., Quay, P. D., Parsons, M. L., Foley, D. G.,
1015 and Seki, M. P. (2003). Influence of a cyclonic eddy on microheterotroph biomass and carbon
1016 export in the lee of Hawaii. *Geophysical Research Letters*, 30(6).
1017 <https://doi.org/10.1029/2002GL016393>
1018

1019 Böttjer, D., Dore, J. E., Karl, D. M., Letelier, R. M., Mahaffey, C., Wilson, S. T., Zehr, J. P., and
1020 Church, M. J. (2016). Temporal variability of nitrogen fixation and particulate nitrogen export at
1021 Station ALOHA. *Limnology and Oceanography*, 62(1), 200-216.
1022 <https://doi.org/10.1002/lno.10386>
1023

1024 Brzezinski, M. A., and Nelson, D. M. (1989). Seasonal changes in the silicon cycle within a Gulf
1025 Stream warm-core ring. *Deep-Sea Research Part A. Oceanographic Research Papers*, 36(7),
1026 1009-1030. [https://doi.org/10.1016/0198-0149\(89\)90075-7](https://doi.org/10.1016/0198-0149(89)90075-7)
1027

1028 Carpenter, J. H. (1965). The accuracy of the Winkler method for dissolved oxygen analysis.
1029 *Limnology and Oceanography*, 10(1), 135-140. <https://doi.org/10.4319/lo.1965.10.1.0135>
1030

1031 Casciotti, K. L., Trull, T. W., Glover, D. M., & Davies, D. (2008). Constraints on nitrogen
1032 cycling at the subtropical North Pacific Station ALOHA from isotopic measurements of nitrate
1033 and particulate nitrogen. *Deep-Sea Research Part II: Topical Studies in Oceanography*, 55(14-

1034 15), 1661-1672. <https://doi.org/10.1016/j.dsr2.2008.04.017>

1035

1036 Chelton, D. B., Schlax, M. G., Samelson, R. M., and de Szoeke, R. A. (2007). Global
1037 observations of large oceanic eddies. *Geophysical Research Letters*, 34(15).
1038 <https://doi.org/10.1029/2007GL030812>

1039

1040 Chelton, D. B., Gaube, P., Schlax, M. G., Early, J. J., and Samelson, R. M. (2011). The influence
1041 of nonlinear mesoscale eddies on near-surface oceanic chlorophyll. *Science*, 334, 328–332.
1042 <https://doi.org/10.1126/science.1208897>

1043

1044 Church, M. J., Mahaffey, C., Letelier, R. M., Lukas, R., Zehr, J. P., and Karl, D. M. (2009).
1045 Physical forcing of nitrogen fixation and diazotroph community structure in the North Pacific
1046 subtropical gyre. *Global Biogeochemical Cycles*, 23. <https://doi.org/10.1029/2008GB003418>

1047

1048 Cullen, J. J. (2015). Subsurface chlorophyll maximum layers: enduring enigma or mystery
1049 solved?. *Annual Review of Marine Science*, 7, 207–239. [https://doi.org/10.1146/annurev-marine-](https://doi.org/10.1146/annurev-marine-010213-135111)
1050 [010213-135111](https://doi.org/10.1146/annurev-marine-010213-135111)

1051

1052 Cullen, J. J., and Eppley, R. W. (1981). Chlorophyll maximum layers of the Southern California
1053 Bight and possible mechanisms of their formation and maintenance. *Oceanologica Acta*, 4(1),
1054 23–32.

1055

1056 Davis, C. S., and McGillicuddy, D. J. (2006). Transatlantic abundance of the N₂-fixing colonial

1057 cyanobacterium *Trichodesmium*. *Science*, 312(5779), 1517-1520.
1058 <https://doi.org/10.1126/science.1123570>
1059
1060 Dore, J. E., Houlihan, T., Hebel, D. V., Tien, G., Tupas, L., and Karl, D. M. (1996). Freezing as a
1061 method of sample preservation for the analysis of dissolved inorganic nutrients in seawater.
1062 *Marine Chemistry*, 541; 53. [https://doi.org/10.1016/0304-4203\(96\)00004-7](https://doi.org/10.1016/0304-4203(96)00004-7).
1063
1064 Dore, J. E., Brum, J. R., Tupas, L. M., and Karl, D. M. (2002). Seasonal and interannual
1065 variability in sources of nitrogen supporting export in the oligotrophic subtropical North Pacific
1066 Ocean. *Limnology and Oceanography*, 47(6), 1595-1607.
1067 <https://doi.org/10.4319/lo.2002.47.6.1595>
1068
1069 Dugenne, M., Henderikx Freitas, F., Wilson, S. T., Karl, D. M., and White, A. E. (2020). Life
1070 and death of *Crocospaera* sp. in the Pacific Ocean: Fine scale predator–prey dynamics.
1071 *Limnology and Oceanography*, 65, 2603–2617. <https://doi.org/10.1002/lno.11473>
1072
1073 Dutkiewicz, S., Hickman, A. E., Jahn, O., Gregg, W. W., Mouw, C. B., and Follows, M. J.
1074 (2015). Capturing optically important constituents and properties in a marine biogeochemical and
1075 ecosystem model. *Biogeosciences*, 12, 4447–4481. <https://doi.org/10.5194/bg-12-4447-2015>
1076
1077 Emerson, S., and Hayward, T. L. (1995). Chemical tracers of biological processes in shallow
1078 waters of North Pacific: preformed nitrate distributions. *Journal of Marine Research*, 53(3), 499-
1079 513, <https://doi.org/10.1357/0022240953213179>

1080

1081 Falkowski, P. G., Ziemann, D., Kolber, Z., and Bienfang, P. K. (1991). Role of eddy pumping in
1082 enhancing primary production in the ocean. *Nature*, 352(6330), 55-58.
1083 <https://doi.org/10.1038/352055a0>

1084

1085 Fawcett, S. E., Johnson, K. S., Riser, S. C., Van Oostende, N., and Sigman, D. M. (2018). Low-
1086 nutrient organic matter in the Sargasso Sea thermocline: A hypothesis for its role, identity, and
1087 carbon cycle implications. *Marine Chemistry*, 207: 108-123.
1088 <https://doi.org/10.1016/j.marchem.2018.10.008>

1089

1090 Fong, A. A., Karl, D. M., Lukas, R., Letelier, R. M., Zehr, J. P., & Church, M. J. (2008).
1091 Nitrogen fixation in an anticyclonic eddy in the oligotrophic North Pacific Ocean. *The ISME*
1092 *journal*, 2(6), 663-676. <https://doi.org/10.1038/ismej.2008.22>

1093

1094 Foreman, R. K., Segura-Noguera, M., and Karl, D. M. (2016). Validation of Ti(III) as a reducing
1095 agent in the chemiluminescent determination of nitrate and nitrite in seawater. *Marine Chemistry*,
1096 186: 83-9. <https://doi.org/10.1016/j.marchem.2016.08.003>

1097

1098 Gaube, P., D. J. McGillicuddy, D. B. Chelton, M. J. Behrenfeld, and P. G. Strutton, (2014).
1099 Regional variations in the influence of mesoscale eddies on near-surface chlorophyll, *Journal of*
1100 *Geophysical Research: Oceans*, 119, 8195–8220. <https://doi.org/10.1002/2014JC010111>

1101

1102 Goldman, J. C. (1993). Potential role of large oceanic diatoms in new primary production. *Deep-*

1103 *Sea Research Part I: Oceanographic Research Papers*, 40(1), 159-168.
1104 [https://doi.org/10.1016/0967-0637\(93\)90059-C](https://doi.org/10.1016/0967-0637(93)90059-C)
1105
1106 Goldman, J.C., and McGillicuddy, D. Jr J. (2003). Effect of large marine diatoms growing at low
1107 light on episodic new production. *Limnology and Oceanography*, 48, 1176-1182.
1108 <https://doi.org/10.4319/lo.2003.48.3.1176>
1109
1110 Grabowski, E., Letelier, R. M., Laws, E. A., and Karl, D. M. (2019). Coupling carbon and energy
1111 fluxes in the North Pacific Subtropical Gyre. *Nature Communications*, 10(1), 1-9.
1112 <https://doi.org/10.1038/s41467-019-09772-z>
1113
1114 Guo, M., Xiu, P., Chai, F., and Xue, H. (2019). Mesoscale and submesoscale contributions to
1115 high sea surface chlorophyll in subtropical gyres, *Geophysical Research Letters*, 46(22), 13217-
1116 13226. <https://doi.org/10.1029/2019GL085278>
1117
1118 Herbland, A., and Voituriez, B. (1979). Hydrological structure analysis for estimating the
1119 primary production in the tropical Atlantic Ocean. *Journal of Marine Research*, 37(1), 87–101.
1120
1121 Hogle, S. L., Dupont, C. L., Hopkinson, B. M., King, A. L., Buck, K. N., Roe, K. L., Stuart, R.
1122 K., Allen, A. E., Mann, E. L., Johnson, Z. I., and Barbeau, K. A (2018). Pervasive iron limitation
1123 at subsurface chlorophyll maxima of the California Current. *Proceedings of the National*
1124 *Academy of Sciences*, 115(52), 13300-13305. <https://doi.org/10.1073/pnas.1813192115>
1125

1126 Johnson, K. S., Riser, S. C., and Karl, D. M. (2010). Nitrate supply from deep to near-surface
1127 waters of the North Pacific subtropical gyre. *Nature*, 465(7301), 1062-1065.
1128 <https://doi.org/10.1038/nature09170>
1129
1130 Karl, D. M., Bidigare, R. R., and Letelier, R. M. (2001). Long-term changes in plankton
1131 community structure and productivity in the North Pacific Subtropical Gyre: The domain shift
1132 hypothesis, *Deep-Sea Research Part II: Topical Studies in Oceanography*, 48, 1449–1470.
1133 [https://doi.org/10.1016/S0967-0645\(00\)00149-1](https://doi.org/10.1016/S0967-0645(00)00149-1)
1134
1135 Karl, D. M., Christian, J. R., Dore, J. E., Hebel, D. V., Letelier, R. M., Tupas, L. M., and Winn,
1136 C. D. (1996). Seasonal and interannual variability in primary production and particle flux at
1137 Station ALOHA. *Deep-Sea Research Part II: Topical Studies in Oceanography*, 43(2-3), 539-
1138 568. [https://doi.org/10.1016/0967-0645\(96\)00002-1](https://doi.org/10.1016/0967-0645(96)00002-1)
1139
1140 Karl, D. M. (1999). A sea of change: biogeochemical variability in the North Pacific Subtropical
1141 Gyre. *Ecosystems*, 2(3), 181-214. <https://doi.org/10.1007/s100219900068>
1142
1143 Karl, D., Letelier, R., Tupas, L., Dore, J., Christian, J., and Hebel, D. (1997). The role of nitrogen
1144 fixation in biogeochemical cycling in the subtropical North Pacific Ocean. *Nature*, 388(6642),
1145 533-538. <https://doi.org/10.1038/41474>
1146
1147 Knauer, G. A., Martin, J. H., and Bruland, K. W. (1979). Fluxes of particulate carbon, nitrogen,
1148 and phosphorus in the upper water column of the northeast Pacific. *Deep-Sea Research Part A*.

1149 *Oceanographic Research Papers*, 26(1), 97-108. [https://doi.org/10.1016/0198-0149\(79\)90089-X](https://doi.org/10.1016/0198-0149(79)90089-X)
1150

1151 Kuwahara, V. S., Nencioli, F., Dickey, T. D., Rii, Y. M., and Bidigare, R. R. (2008). Physical
1152 dynamics and biological implications of Cyclone Noah in the lee of Hawai'i during E-Flux I.
1153 *Deep-Sea Research Part II: Topical Studies in Oceanography*, 55, 1231-1251.
1154 <https://doi.org/10.1016/j.dsr2.2008.01.007>
1155

1156 Letelier, R. M., Karl, D. M., Abbott, M. R., Flament, P., Freilich, M., Lukas, R., and Strub, T.
1157 (2000). Role of late winter mesoscale events in the biogeochemical variability of the upper water
1158 column of the North Pacific Subtropical Gyre. *Journal of Geophysical Research: Oceans*, 105,
1159 28723–39. <https://doi.org/10.1029/1999JC000306>
1160

1161 Letelier, R. M., Karl, D. M., Abbott, M. R., & Bidigare, R. R. (2004). Light driven seasonal
1162 patterns of chlorophyll and nitrate in the lower euphotic zone of the North Pacific Subtropical
1163 Gyre. *Limnology and Oceanography*, 49, 508–519. <https://doi.org/10.4319/lo.2004.49.2.0508>
1164

1165 Letscher, R. T., and Villareal, T. A. (2018). Evaluation of the seasonal formation of subsurface
1166 negative preformed nitrate anomalies in the subtropical North Pacific and North Atlantic.
1167 *Biogeosciences*, 15(21), 6461-6480. <https://doi.org/10.5194/bg-15-6461-2018>
1168

1169 Lewis, M. R., Hebert, D., Harrison, W. G., Platt, T., and Oakey, N. S. (1986). Vertical nitrate
1170 fluxes in the oligotrophic ocean. *Science*, 234(4778), 870–873.
1171 <https://doi.org/10.1126/science.234.4778.870>

1172

1173 Li, B., Karl, D. M., Letelier, R. M., and Church, M. J. (2011). Size-dependent photosynthetic
1174 variability in the North Pacific Subtropical Gyre. *Marine Ecology Progress Series*, 440, 27–40.
1175 <https://doi.org/10.3354/meps09345>

1176

1177 Li, B., Karl, D. M., Letelier, R. M., Bidigare, R. R., and Church, M. J. (2013). Variability of
1178 chromophytic phytoplankton in the North Pacific Subtropical Gyre. *Deep-Sea Research Part II:
1179 Topical Studies in Oceanography*, 93, 84-95. <https://doi.org/10.1016/j.dsr2.2013.03.007>

1180

1181 Mackas, D. L., Denman, K. L., and Abbott, M. R. (1985). Plankton patchiness: biology in the
1182 physical vernacular. *Bulletin of Marine Science*, 37(2), 652-674.

1183

1184 Malmstrom, R. R., Coe, A., Kettler, G. C., Martiny, A. C., Frias-Lopez, J., Zinser, E. R., and
1185 Chisholm, S. W. (2010). Temporal dynamics of *Prochlorococcus* ecotypes in the Atlantic and
1186 Pacific oceans. *The ISME journal*, 4, 1252–64. <https://doi.org/10.1038/ismej.2010.60>

1187

1188 Marshall, J., Hill, C., Perelman, L., and Adcroft, A. (1997). Hydrostatic, quasi-hydrostatic, and
1189 nonhydrostatic ocean modeling. *Journal of Geophysical Research: Oceans*, 102, 5733–5752.
1190 <https://doi.org/10.1029/96JC02776>

1191

1192 McClain, C. R., Signorini, S. R., and Christian, J. R. (2004). Subtropical gyre variability
1193 observed by ocean-color satellites. *Deep Sea Research Part II: Topical Studies in Oceanography*,
1194 51(1-3), 281-301. <https://doi.org/10.1016/j.dsr2.2003.08.002>

1195

1196 McGillicuddy Jr, D. J., Johnson, R. J., Siegel, D. A., Michaels, A. F., Bates, N., and Knap, A. H.
1197 (1999). Mesoscale variations of biogeochemical properties in the Sargasso Sea. *Journal of*
1198 *Geophysical Research: Oceans*, 104, 13381-13394. <https://doi.org/10.1029/1999JC900021>
1199

1200 McGillicuddy Jr, D. J., and Robinson, A. R. (1997). Eddy-induced nutrient supply and new
1201 production in the Sargasso Sea. *Deep-Sea Research Part I: Oceanographic Research Papers*, 44,
1202 1427–1450. [https://doi.org/10.1016/S0967-0637\(97\)00024-1](https://doi.org/10.1016/S0967-0637(97)00024-1)
1203

1204 Menden-Deuer, S., and Lessard, E. J. (2000). Carbon to volume relationships for dinoflagellates,
1205 diatoms, and other protist plankton. *Limnology and Oceanography* 45, 569-579.
1206 <https://doi.org/10.4319/lo.2000.45.3.0569>
1207

1208 Munk, W. (2002). The evolution of physical oceanography in the last hundred years.
1209 *Oceanography*, 15(1), 135-142. <https://doi.org/10.5670/oceanog.2002.45>
1210

1211 Pedlosky, J. (1990). The dynamics of the oceanic subtropical gyres. *Science*, 248(4953), 316-322.
1212 <https://doi.org/10.1126/science.248.4953.316>
1213

1214 Raven, J. A., and Crawford, K. (2012). Environmental controls on coccolithophore calcification.
1215 *Marine Ecology Progress Series*, 470, 137-166. <https://doi.org/10.3354/meps09993>
1216

1217 Redfield, A. C. (1958). The biological control of chemical factors in the environment. *American*

1218 *scientist*, 46(3), 205-222.

1219

1220 Rii, Y. M., Brown, S. L., Nencioli, F., Kuwahara, V., Dickey, T., Karl, D. M., and Bidigare, R. R.

1221 (2008). The transient oasis: Nutrient-phytoplankton dynamics and particle export in Hawaiian lee

1222 cyclones. *Deep-Sea Research Part II: Topical Studies in Oceanography*, 55(10–13), 1275–1290.

1223 <https://doi.org/10.1016/j.dsr2.2008.01.013>

1224

1225 Roesler, C., Uitz, J., Claustre, H., Boss, E., Xing, X., Organelli, E., ... and Barbieux, M. (2017).

1226 Recommendations for obtaining unbiased chlorophyll estimates from in situ chlorophyll

1227 fluorometers: A global analysis of WET Labs ECO sensors. *Limnology and Oceanography: Methods*,

1228 15(6), 572–585. <https://doi.org/10.1002/lom3.10185>

1229

1230 Scharek, R., Latasa, M., Karl, D. M., and Bidigare, R. R. (1999). Temporal variations in diatom

1231 abundance and downward vertical flux in the oligotrophic North Pacific gyre. *Deep-Sea Research*

1232 *Part I: Oceanographic Research Papers*, 46(6), 1051-1075. [https://doi.org/10.1016/S0967-](https://doi.org/10.1016/S0967-0637(98)00102-2)

1233 [0637\(98\)00102-2](https://doi.org/10.1016/S0967-0637(98)00102-2)

1234

1235 Schlax, M. G., and Chelton, D. B. (2016). The “Growing Method” of Eddy Identification and

1236 Tracking in Two and Three Dimensions. *Corvallis: College of Earth, Ocean and Atmospheric*

1237 *Sciences, Oregon State University*.

1238

1239 Sosik, H. M., and Olson, R. J. (2007). Automated taxonomic classification of phytoplankton

1240 sampled with imaging in flow cytometry. *Limnology and Oceanography: Methods*, 5, 204-216.

1241 <https://doi.org/10.4319/lom.2007.5.204>

1242

1243 Strickland, J. D. H., and Parsons, T. R. (1972). A practical handbook of seawater analysis.

1244 *Fisheries Research Board of Canada*, 2nd edition. <https://doi.org/10.1002/iroh.19700550118>

1245

1246 Sweeney, E. N., McGillicuddy Jr, D. J., and Buesseler, K. O. (2003). Biogeochemical impacts

1247 due to mesoscale eddy activity in the Sargasso Sea as measured at the Bermuda Atlantic Time-

1248 series Study (BATS). *Deep-Sea Research Part II: Topical Studies in Oceanography*, 50(22–26),

1249 3017–3039. <https://doi.org/10.1016/j.dsr2.2003.07.008>

1250

1251 Vaillancourt, R. D., Marra, J., Seki, M. P., Parsons, M. L., and Bidigare, R. R. (2003). Impact of

1252 a cyclonic eddy on phytoplankton community structure and phytoplankton competency in the

1253 subtropical North Pacific Ocean. *Deep-Sea Research Part I: Oceanographic Research Papers*,

1254 50, 829-847. [https://doi.org/10.1016/S0967-0637\(03\)00059-1](https://doi.org/10.1016/S0967-0637(03)00059-1)

1255

1256 Venrick, E. L. (1982). Phytoplankton in an oligotrophic ocean: observations and questions.

1257 *Ecological Monographs*, 52, 129–154. <https://doi.org/10.2307/1942608>

1258

1259 Venrick, E. L. (1990). Mesoscale patterns of chlorophyll *a* in the central North Pacific. *Deep-Sea*

1260 *Research Part A. Oceanographic Research Papers*, 37(6), 1017-1031.

1261 [https://doi.org/10.1016/0198-0149\(90\)90108-8](https://doi.org/10.1016/0198-0149(90)90108-8)

1262

1263 Venrick, E. L. (1999). Phytoplankton species structure in the central North Pacific 1973-1996:

1264 variability and persistence, *Journal of Plankton Research*, 21, 1029–1042.
1265 <https://doi.org/10.1093/plankt/21.6.1029>
1266
1267 Villareal, T., Altabet, M., and Culver-Rymsza, K. (1993). Nitrogen transport by vertically
1268 migrating diatom mats in the North Pacific Ocean. *Nature* **363**, 709–712.
1269 <https://doi.org/10.1038/363709a0>
1270
1271 Wilson, S., del Valle, D., Segura-Noguera, M., and Karl, D. (2014). A role for nitrite in the
1272 production of nitrous oxide in the lower euphotic zone of the oligotrophic North Pacific Ocean.
1273 *Deep-Sea Research Part I: Oceanographic Research Papers*, 85, 47-55.
1274 [10.1016/j.dsr.2013.11.008](https://doi.org/10.1016/j.dsr.2013.11.008).
1275
1276 Wilson, S. T., Aylward, F. O., Ribalet, F., Barone, B., Casey, J. R., Connell, P. E., ... and
1277 DeLong, E. F. (2017). Coordinated regulation of growth, activity and transcription in natural
1278 populations of the unicellular nitrogen-fixing cyanobacterium *Crocospaera*. *Nature*
1279 *Microbiology*, 2(9), 1-9. <https://doi.org/10.1038/nmicrobiol.2017.118>
1280
1281 Wunsch, C. (1997). The vertical partition of oceanic horizontal kinetic energy. *Journal of*
1282 *Physical Oceanography*, 27, 1770–1794. [https://doi.org/10.1175/1520-](https://doi.org/10.1175/1520-0485(1997)027<1770:TVPOOH>2.0.CO;2)
1283 [0485\(1997\)027<1770:TVPOOH>2.0.CO;2](https://doi.org/10.1175/1520-0485(1997)027<1770:TVPOOH>2.0.CO;2)